
8

REFLECTOR ANTENNAS

The importance of reflector antennas cannot be overstated. Large-aperture antennas can be built only with reflectors or arrays and reflectors are far simpler than arrays. The arrays give us more degrees of freedom than is necessary in many applications. With plenty of room and slow scan rates, a reflector becomes a better design than an array. Of course, there can be many valid reasons for using an array in an application, but a reflector should always be considered. An array needs an elaborate feed network, whereas a reflector uses a simple feed and free space as its feed network.

Most reflector designs require extensive calculations together with full characterization of the feed antenna. Many types of analysis have been developed. As with horn antennas, Love [1] has collected significant papers on reflector antennas. In his classic book, Silver [2] provides the foundation for an analysis based on aperture theory and physical optics (induced currents on the reflector). Aperture theory or physical optics reduced to aperture theory is still used for most designs. Rusch and Potter fully develop aperture and physical optics theories for the design and analysis of both prime focus and dual-reflector (Cassegrain) antennas [3]. Other methods have been developed either to increase the range of valid patterns or to decrease the pattern calculation time so that optimization techniques can be applied. Wood [4] collects ideas for designing by using spherical wave expansions that allow for an overall system optimization using only a few terms. GTD methods [5,6] find increasing applications as an analysis technique suitable for a full pattern analysis except at boresight. Improved methods of calculating the secondary pattern have been developed using aperture fields, such as FFT methods [7] and Jacobi–Bessel series [8]. Many of these techniques and hardware implementations of reflectors are summarized in a handbook [9, Chaps. 2 and 3]. Although all these methods are available, aperture theory and physical optics remain the main techniques of reflector design and analysis.

8-1 PARABOLOIDAL REFLECTOR GEOMETRY

Figure 8-1 shows the geometry of the parabolic reflector. We form the reflector by rotating the figure about its axis or by moving the figure along an axis out of the paper to form a cylindrical reflector. Because the cylindrical reflector requires a line source, it is less important than the circularly symmetrical reflector fed from a single point source. A paraboloidal reflector transforms a spherical wave radiated by the feed located at its focus into a plane wave. Although the feed wave spreads from the focus, which reduces its amplitude, geometric optics predicts a plane wave reflection that remains constant. The reflected wave does not remain a plane wave but spreads because the fields must be continuous across the reflection boundary of the beam plane wave column because fields can be discontinuous only across physical boundaries. Nevertheless, we will use the aperture theory on the projected diameter to predict its performance. Since the reflected rays are parallel, we can place the aperture plane anywhere along the axis, but somewhat close in front of the reflector. The equations for the reflector surface are

$$\begin{array}{ll} r^2 = 4f(f + z) & \rho = \frac{f}{\cos^2(\psi/2)} \\ \text{rectangular} & \text{polar} \\ \text{coordinates} & \text{coordinates} \end{array} \quad (8-1)$$

where f is the focal length, D the diameter, ρ the distance from the focus to the reflector, and ψ the feed angle from the negative z -axis. The reflector depth from the rim to the center is $z_0 = D^2/16f$.

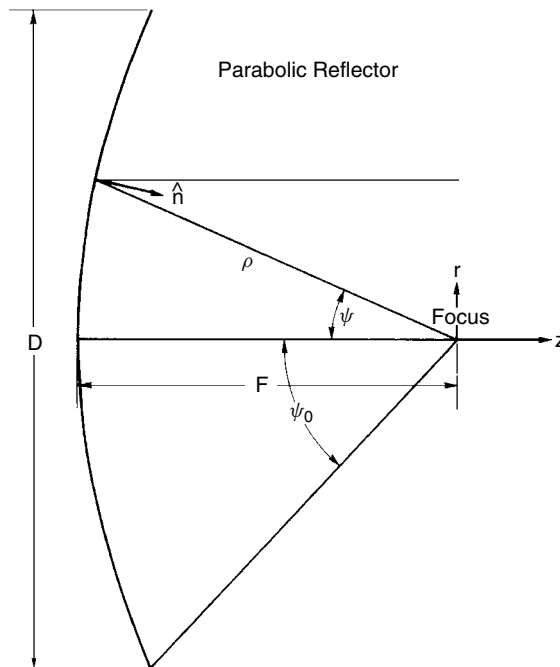
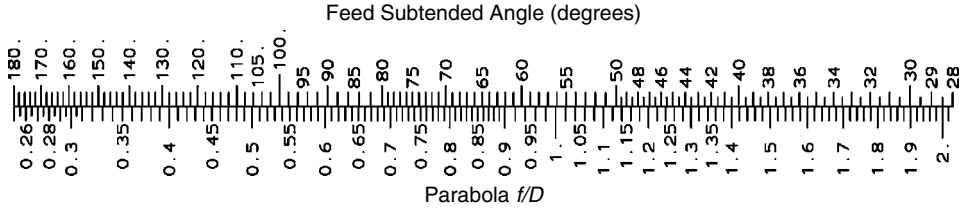


FIGURE 8-1 Geometry of a parabolic reflector.



SCALE 8-1 Parabola f/D compared to a feed total subtended angle.

We eliminate the dimensions of the reflector by using the ratio f/D . The half subtended angle of the reflector, ψ_0 , relates to f/D by

$$\psi_0 = 2 \tan^{-1} \frac{1}{4f/D} \quad (8-2)$$

Scale 8-1 computes the total feed subtended angle from reflector f/D . When we place the aperture plane at the focus, the ray path distance becomes

$$\rho + \rho \cos \psi = 2\rho \cos^2 \frac{\psi}{2} = 2f$$

all ray path lengths are equal, and the aperture plane is a constant-phase surface (eikonal).

The normal unit vector at a point on the reflector (r, z) is found from the feed angle:

$$\hat{\mathbf{n}} = -\sin \frac{\psi}{2} \hat{\mathbf{r}} + \cos \frac{\psi}{2} \hat{\mathbf{z}}$$

At this point we need the radius of curvatures in the principal planes to apply Eq. (2-77) reflection from a curved surface: R_1 in the r - z plane and R_2 in the ϕ - z plane:

$$R_1 = \frac{2f}{\cos^3(\psi/2)} \quad \text{and} \quad R_2 = \frac{2f}{\cos(\psi/2)}$$

The spherical wave spreads from the feed as $1/\rho$. At the surface of the reflector the wave curvature changes to a plane wave and propagates to the aperture plane at a constant amplitude. The spherical wave spreading multiplies the feed distribution by [Eq. (8-1)] $\cos^2(\psi/2)$ in the aperture. Then

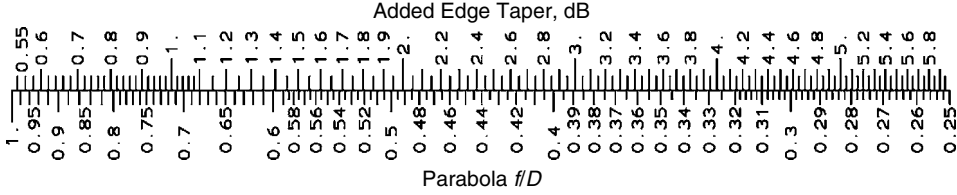
$$\text{added edge taper} = \cos^2 \frac{\psi_0}{2} \quad \text{voltage} \quad (8-3)$$

Deeper reflectors (smaller f/D) have greater edge tapers than shallow reflectors (larger f/D). Scale 8-2 provides a quick calculation of the added edge taper due to spherical wave spreading.

Example Calculate the edge taper of a paraboloidal reflector for $f/D = 0.5$ and an isotropic feed.

From Eq. (8-2), $\psi_0 = 2 \tan^{-1} \frac{1}{2} = 53.13^\circ$. The edge taper is [Eq. (8-3)]

$$\text{edge taper} = 20 \log \cos^2 \frac{53.13^\circ}{2} = -1.94 \text{ dB}$$



SCALE 8-2 Added edge taper due to a spherical wave from feed.

If the feed has its 10-dB pattern point directed toward the reflector edge, the aperture edge taper is 11.9 dB.

8-2 PARABOLOIDAL REFLECTOR APERTURE DISTRIBUTION LOSSES

We manipulate Eq. (4-2) for ATL to eliminate the dimensions and relate the integrals to the feed pattern:

$$\text{ATL} = \frac{\left[\int_0^{2\pi} \int_b^a |E_a(r', \phi')| r' dr' d\phi' \right]^2}{\pi a^2 \int_0^{2\pi} \int_b^a |E_a(r', \phi')|^2 r' dr' d\phi'} \quad (8-4)$$

where a is the aperture radius, b the central blockage radius, and $E_a(r', \phi')$ the aperture field. We make the following substitutions into Eq. (8-4):

$$\begin{aligned} r' &= \rho \sin \psi = 2 \sin \frac{\psi}{2} \cos \frac{\psi}{2} \frac{f}{\cos^2(\psi/2)} = 2f \tan \frac{\psi}{2} \\ dr' &= f \sec^2 \frac{\psi}{2} = \rho d\psi \end{aligned} \quad (8-5)$$

The aperture field is related to the feed pattern by

$$E_a(r', \phi') = \frac{E(\psi', \phi')}{\rho}$$

These substitutions eliminate dimensions in Eq. (8-4):

$$\text{ATL} = \frac{\left[\int_0^{2\pi} \int_{\psi_b}^{\psi_0} |E(\psi, \phi)| \tan(\psi/2) d\psi d\phi \right]^2}{\pi [\tan^2(\psi_0/2) - \tan^2(\psi_b/2)] \int_0^{2\pi} \int_{\psi_b}^{\psi_0} |E(\psi, \phi)|^2 \sin \psi d\psi d\phi} \quad (8-6)$$

where $\psi_b = 2 \tan^{-1}[b/(2f)]$. When we substitute the relations in Eq. (8-5) into Eq. (4-9) to eliminate dimensions in the integrals, we obtain an expression with only the feed

pattern:

$$\text{PEL} = \frac{\left| \int_0^{2\pi} \int_{\psi_b}^{\psi_0} E(\psi, \phi) \tan(\psi/2) d\psi d\phi \right|^2}{\left[\int_0^{2\pi} \int_{\psi_b}^{\psi_0} |E(\psi, \phi)| \tan(\psi/2) d\psi d\phi \right]^2} \quad (8-7)$$

PEL is the efficiency at the boresight. We modify Eq. (8-7) when we scan the beam to give off-boresight values as in Eq. (4-3).

The amplitude taper efficiency (ATL) of Eq. (8-6) and the phase error efficiency (PEL) of Eq. (8-7) do not account for the total directivity loss of the aperture. The reflector does not intercept all the power radiated by the source and some of it spills over the edge. Spillover adds little to the pattern except as sidelobes, since usual feeds have small backlobes. We consider this spilled-over power as a loss (SPL):

$$\text{SPL} = \frac{\int_0^{2\pi} \int_{\psi_b}^{\psi_0} |E(\psi, \phi)|^2 \sin \psi d\psi d\phi}{\int_0^{2\pi} \int_0^{\pi} |E(\psi, \phi)|^2 \sin \psi d\psi d\phi} \quad (8-8)$$

This expression for spillover includes the scattered portion of the central blockage efficiency, but not the loss of potential aperture. We include the remainder in the directivity calculation.

We have ignored the cross-polarized power radiated by the source. We define cross-polarization efficiency (XOL) as

$$\text{XOL} = \frac{\int_0^{2\pi} \int_0^{\pi} |E_C(\psi, \phi)|^2 \sin \psi d\psi d\phi}{\int_0^{2\pi} \int_0^{\pi} (|E_C(\psi, \phi)|^2 + |E_X(\psi, \phi)|^2) \sin \psi d\psi d\phi} \quad (8-9)$$

where E_C is the co-polarized field and E_X is the cross-polarized field. These polarizations correspond to Ludwig's [10] third definition of cross-polarization. A Huygens source produces straight reflector surface currents when projected to the aperture plane. Including the cross-polarization efficiency gives us the true average radiation intensity as in Eq. (1-17).

If we express the efficiencies as ratios, the directivity will be found from

$$\text{directivity} = \left(\frac{\pi}{\lambda} \right)^2 (D_r^2 - D_b^2) \text{SPL} \cdot \text{ATL} \cdot \text{PEL} \cdot \text{XOL} \quad (\text{ratio}) \quad (8-10)$$

where D_r is the reflector diameter and D_b is the diameter of the central blockage. Equation (8-10) includes the nonscattered blockage loss of potential aperture. Equation (8-10) can be expressed in terms of decibel ratios:

$$\begin{aligned} \text{directivity} = 10 \log \left[\left(\frac{\pi}{\lambda} \right)^2 (D_r^2 - D_b^2) \right] &+ \text{SPL(dB)} + \text{ATL(dB)} \\ &+ \text{PEL(dB)} + \text{XOL(dB)} \end{aligned} \quad (8-11)$$

Of course, all the decibel ratios of the efficiencies will be negative and subtract from the directivity calculated from the area.

When measuring an actual feed, we can ignore the cross-polarized power. We measure the efficiency as the difference between directivity and gain. Actual directivity includes the co-polarizations and cross-polarizations in the average radiation intensity. If we ignore the cross-polarization, the measured efficiency decreases by the cross-polarization loss because the measured and true directivity differ by that loss. We must measure the cross-polarization pattern distribution of the feed if we want to calculate the cross-polarized secondary (reflector) pattern. When the cross-polarization pattern is not required, we save time without loss of accuracy by measuring only the co-polarized feed pattern.

Equations (8-8) and (8-9) are by no means unique. We could include the cross-polarized power in the spillover calculation [Eq. (8-8)] and limit the integration limits in Eq. (8-9) to the reflector. A set of efficiency relations is correct when the equations account for all the power radiated by the feed. When we use calculated feed patterns, we must determine cross-polarization efficiency, since we can only estimate the efficiency due to material losses. The cross-polarization efficiency cannot be included as it is in measurements, and the division of cross-polarized power between Eqs. (8-8) and (8-9) is arbitrary.

8-3 APPROXIMATE SPILLOVER AND AMPLITUDE TAPER TRADE-OFFS

We use the approximate pattern $\cos^{2N}(\psi/2)$ for a feed pattern to establish trends. Of course, if the actual feed pattern distribution is available, we should use Eqs. (8-6) to (8-9). We obtain closed-form expressions when we substitute this pattern into Eqs. (8-6) and (8-8). Ignoring any central blockage, we get

$$\text{spillover efficiency} = 1 - u^{2(N+1)} \quad (8-12)$$

$$\text{amplitude taper efficiency} = \frac{4(N+1)(1-u^N)^2}{N^2[1-u^{2(N+1)}]} \cot^2 \frac{\psi_0}{2} \quad (8-13)$$

where $u = \cos(\psi_0/2)$. We combine Eqs. (8-12) and (8-13) and plot their combination to find the beamwidth for minimum loss. In Figure 8-2 the loss versus the 10-dB beamwidth for various f/D values is plotted. At narrow beamwidths little feed power spills over the reflector edge, but the reflector is underilluminated. Increasing the beamwidth improves the illumination but increases the spillover. The efficiency peaks when the feed 10-dB beamwidth is approximately the subtended angle of the reflector. Figure 8-2 shows a broad peak for any given f/D . Small changes in the beamwidth near the peak have no practical effect on the reflector's gain. Scale 8-3 relates the average illumination loss reduction given the feed pattern level in the direction of the reflector rim for typical antennas.

Example Estimate the amplitude taper loss for a reflector with $f/D = 0.5$ whose feed has a 10-dB edge taper.

Compare the loss with that of the circular Gaussian and the Hansen single-parameter distributions: $\psi_0 = 2 \tan^{-1} \frac{1}{2} = 53.13^\circ$. The 10-dB beamwidth of the feed is then 106.26° . We modify Eq. (1-20) to compute the exponent N of the $\cos^{2N}(\psi/2)$ feed

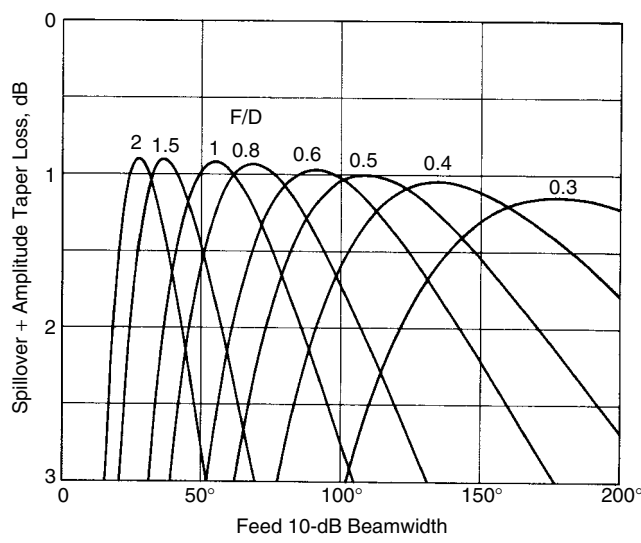
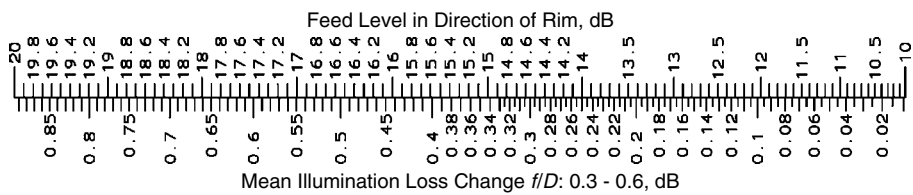


FIGURE 8-2 Sum of spillover and amplitude taper losses versus feed 10-dB beamwidth.



SCALE 8-3 Mean illumination loss change of a reflector given the feed pattern level in the rim direction.

pattern approximation,

$$N = \frac{\log 0.1}{2 \log \cos(106.26^\circ/4)} = 10.32$$

From Eq. (8-13), $u = \cos(53.13^\circ/2) = 0.894$:

$$\begin{aligned} \text{ATL(dB)} &= \frac{4(1 - 0.894^{10.32})^2(11.32)}{10.32^2(1 - 0.894^{22.64})} \cot^2(53.13^\circ/2) = 0.864 \\ &= 10 \log 0.864 = -0.63 \text{ dB} \end{aligned}$$

The extra distance from the feed to the reflector edge compared with the center distance adds 1.94 dB and increases the aperture amplitude taper to 11.94 dB. We interpolate Table 4-29 for the circular Gaussian distribution and Table 4-30 for the Hansen single-parameter distribution to find the following data:

Gaussian	Hansen
ATL(dB) = -0.62 dB	ATL(dB) = -0.57 dB
Sidelobe level = 26.3 dB	Sidelobe level = 24.7 dB
Beamwidth factor = 1.142	Beamwidth factor = 1.136

We multiply Eq. (4-83) by the beamwidth factor to estimate the reflector beamwidth:

$$\text{HPBW} = 67.3^\circ \frac{\lambda}{D} \quad \text{and} \quad \text{HPBW} = 67^\circ \frac{\lambda}{D}$$

These compare well with the approximation, $\text{HPBW} = 70^\circ \lambda/D$ for a parabolic reflector. An integration of the aperture distribution for the far-field pattern gives the following results:

$$\text{HPBW} = 67.46^\circ \frac{\lambda}{D} \quad \text{sidelobe level} = 27 \text{ dB}$$

8-4 PHASE ERROR LOSSES AND AXIAL DEFOCUSING

All rays starting at the reflector focus travel the same distance through reflection to the aperture plane. The aperture plane is any convenient plane in front of the dish whose normal is the axis of the reflector. If we could build a feed with a unique phase center and place it at the focus of a perfect paraboloidal reflector, we would eliminate phase error loss in the aperture plane because it would have a constant phase. The feed, the positioning of the feed, and the reflector surface all contribute to the phase error loss.

We discussed techniques for obtaining unique phase centers in the various planes for horns. Unlike smooth-wall horns, corrugated horns can have equal phase centers in all planes through the axis, but even their position will wander with changes in frequency. We measure the feed pattern distribution (amplitude and phase) to predict the contribution of the feed to the overall efficiency. From those measurements we define the practical phase center as the point on the feed leading to the minimum phase error loss when placed at the focus. The random and systematic phase error contributions can be measured directly on the feed and calculated numerically using Eq. (8-7).

The feed phase center cannot always be placed at the focus. The phase-center location wanders with changes in frequency, and in any wideband application we expect axial defocusing. For example, the location of the phase center of a log-periodic antenna moves toward the apex as frequency increases. Figure 8-3 is a plot of the phase error loss due to axial defocusing. Each feed has its 10-dB beamwidth equal to the reflector subtended angle. Axial defocusing affects deep dishes (lower f/D) more than shallow dishes. We can estimate the axial defocusing phase error loss by approximating the distribution with a quadratic aperture phase distribution. Given z as the axial defocusing, the maximum phase deviation in cycles is

$$S = \frac{z}{\lambda} \left[1 - \cos \left(2 \tan^{-1} \frac{1}{4f/D} \right) \right] \quad (8-14)$$

We combine this with the quadratic phase error loss of the circular Gaussian distribution to estimate the loss. With $z = \lambda$ we obtain a scaling factor for S (Scale 8-4) given z from Eq. (8-14). The scaling factor decreases with increasing f/D .

Example Estimate the phase error loss for $z = 2\lambda$ when $f/D = 0.6$ and the feed 10-dB beamwidth equals the reflector subtended angle.

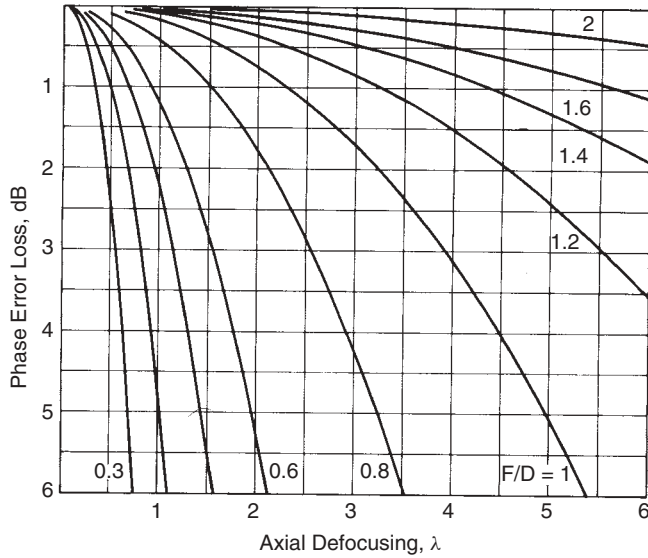
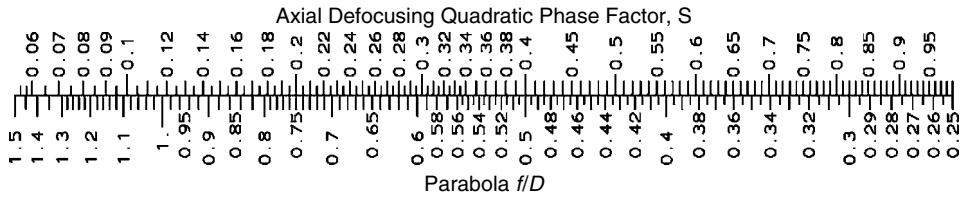


FIGURE 8-3 Paraboloidal reflector phase error loss due to axial defocusing of the feed.



SCALE 8-4 Quadratic phase factor S for axial defocusing of a paraboloidal reflector.

From Scale 8-4, $S = 0.30(2) = 0.60$. We use Eq. (8-3) to compute the edge taper:

$$\psi_0 = 2 \tan^{-1} \frac{1}{2.4} = 45.2^\circ$$

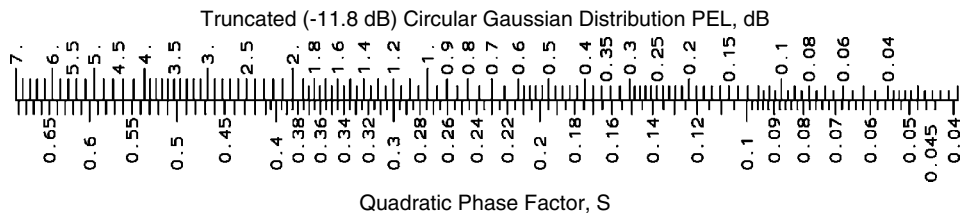
$$\text{edge taper} = 20 \log \cos^2 \frac{\psi_0}{2} = -1.4 \text{ dB}$$

An equivalent truncated Gaussian aperture distribution tapers to

$$10 \text{ dB} + 1.4 \text{ dB} = 11.4 \text{ dB} \quad \rho = \frac{11.4}{8.69} = 1.31$$

We use Eq. (4-118) to calculate phase error efficiency of the truncated Gaussian distribution: $\text{PEL} = 0.305$ or $\text{PEL (dB)} = -5.2 \text{ dB}$. This matches the value from Figure 8-3 found by integration of the actual distribution. The optimum feed beamwidth produces an average aperture edge taper of 11.8 dB. Scale 8-5 evaluates Eq. (4-118) for this taper.

We detect axial defocusing by looking at the patterns of the reflector. Axial defocusing fills-in nulls between sidelobes. We adjust the feed location to maximize the null



SCALE 8-5 Truncated circular Gaussian distribution (−11.8dB taper) phase error loss given S.

depth, but antenna range errors and receiver sensitivity limit our ability to eliminate this defocusing.

8-5 ASTIGMATISM [11]

Both the feed and the reflector can have astigmatism: unequal phase centers in different planes. We measure the feed by itself to discover its astigmatism. When the feed is mounted in the reflector, we detect astigmatism by the depth of nulls in the various pattern planes. A series of measurements can separate the feed and reflector astigmatism, but the feed must be able to move along the reflector axis and to rotate by 90° during the measurements. Move the feed along the axis to find the locations that give maximum nulls. The extrema of the reflector focuses may not occur in the *E*- and *H*-planes and will require a search in the other planes. At this point we cannot separate the feed astigmatism from the reflector astigmatism. We rotate the feed and repeat the measurements. The feed phase center locations shift, and the reflector focuses remain fixed. Simple manipulation of the data from the two measurements separates the two sources of astigmatism. The reflector can be shimmed to remove its astigmatism, or the feed phase centers can be matched to the reflector focuses. Figure 8-4 shows the magnitude

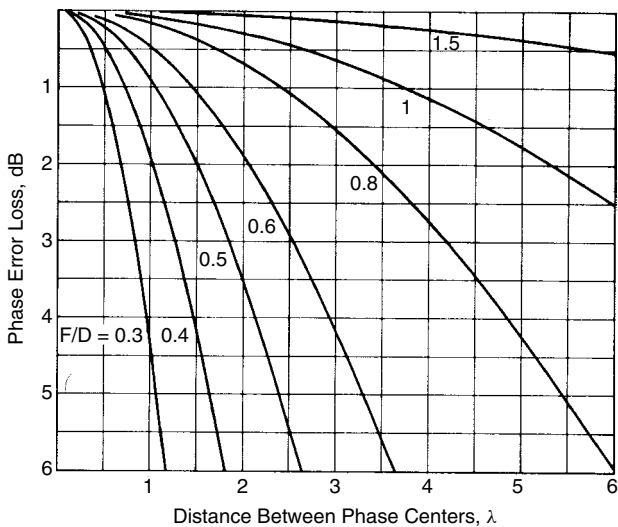


FIGURE 8-4 Paraboloidal reflector phase error loss due to feed astigmatism.

of phase error losses due to feed astigmatism. Astigmatism loss is not as severe as axial defocusing because in two planes the feed phase center is at the reflector focus. As is true of axial defocusing loss, deep dishes are affected more than shallow reflectors.

8-6 FEED SCANNING

Moving the phase center of the feed off axis laterally scans the reflector beam to a limited extent without severe pattern problems. Figure 8-5 shows the k -space pattern effects of feed scanning. The sidelobes show the effects of coma (cubic phase errors) where the sidelobes on the boresight side grow and the sidelobes on the other side decrease. We call these *coma lobes*, although no new lobes are generated. In fact, we see one lobe disappearing as a vestigial lobe with increased scan (Figure 8-5). Suppose that the feed is offset from the axis by a distance d . We measure the offset angle ψ_s from the axis to a line from the feed to the reflector vertex: $d = f \tan \psi_s$. We ignore the slight amplitude distribution change due to the small lateral offset. Referred to the focus, the movement produces a phase factor in the feed pattern: $-kd \sin \psi \cos \phi_c$ when the feed is moved along the negative x -axis.

Equation (8-7) predicts only the boresight phase error loss. Like Eq. (4-3), we must calculate the phase error efficiency at any angle to determine the loss at the pattern peak:

$$\text{PEL}(\theta, \phi) = \frac{\left| \int_0^{2\pi} \int_0^{\psi_0} E(\psi, \phi_c) \tan(\psi/2) e^{jk2f \tan(\psi/2) \sin \theta \cos(\phi - \phi_c)} d\psi d\phi_c \right|^2}{\left[\int \int |E(\psi, \phi_c)| \tan(\psi/2) d\psi d\phi_c \right]^2} \quad (8-15)$$

When we include the offset along $\phi = 0$, the phase factor becomes

$$\exp \left[jkf \cos \phi_c \left(2 \tan \frac{\psi}{2} \sin \theta - \tan \psi_s \sin \psi \right) \right]$$

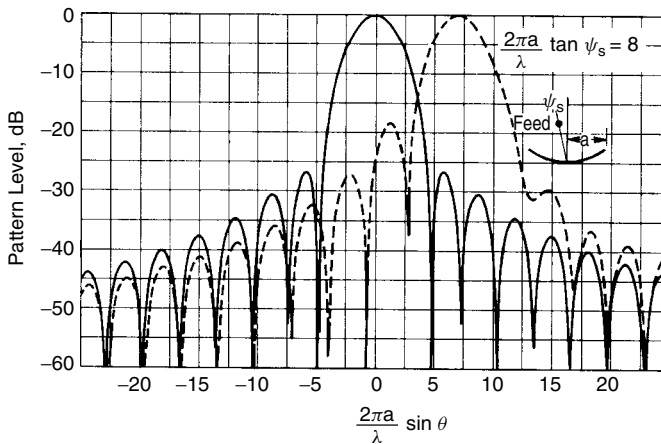


FIGURE 8-5 Feed-scanned paraboloidal reflector $f/D = 0.5$ and feed beamwidth = 60° .

For large reflectors we make the approximations $\psi_s \approx \tan \psi_s$ and $\theta \approx \sin \theta$. The pattern scale and the offset phase factor become $ka\theta$ and $ka\psi_s$.

A flat plate would reflect the ray at an equal angle on the other side of the axis for an offset feed, but a curved reflector modifies that result slightly. The offset factor in Figure 8-5 is 8, and the beam peak is at 7. We call the ratio of the beam maximum to offset angle the beam deviation factor (BDF) [12]:

$$\text{BDF} = \frac{\theta_m}{\psi_s} = \frac{7}{8} \quad \theta_m = \text{BDF} \cdot \psi_s$$

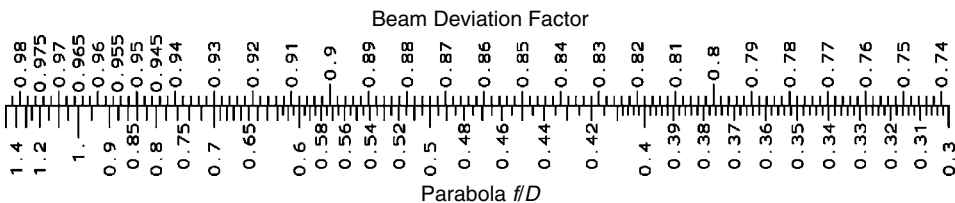
The BDF varies from less than 1 for a concave reflector to greater than 1 for a convex reflector. BDF equals 1 for a flat reflector. Table 8-1 lists the BDF values for various f/D and Scale 8-6 gives the relationship. The BDF approaches 1 as f/D approaches infinity (flat plate). The approximate expression for BDF is

$$\text{BDF} = \frac{(4f/D)^2 + 0.36}{(4f/D)^2 + 1} \quad (8-16)$$

Feed scanning increases the phase error loss. When normalized to beamwidths of scan, a single loss curve can be drawn for each f/D (Figure 8-6). Scanning also raises the sidelobes. Table 8-2 gives the approximate level of the peak coma lobe for a given scan loss. It is almost independent of f/D .

**TABLE 8-1 Feed-Scanned Paraboloidal Reflector
Beam Deviation Factor**

f/D	BDF	f/D	BDF
0.30	0.724	0.80	0.945
0.35	0.778	0.85	0.951
0.40	0.818	0.90	0.957
0.45	0.850	1.00	0.965
0.50	0.874	1.10	0.970
0.55	0.893	1.20	0.975
0.60	0.908	1.40	0.981
0.65	0.921	1.60	0.986
0.70	0.930	1.80	0.989
0.75	0.938	2.00	0.991



SCALE 8-6 Feed-scanned reflector beam deviation factor given f/D .

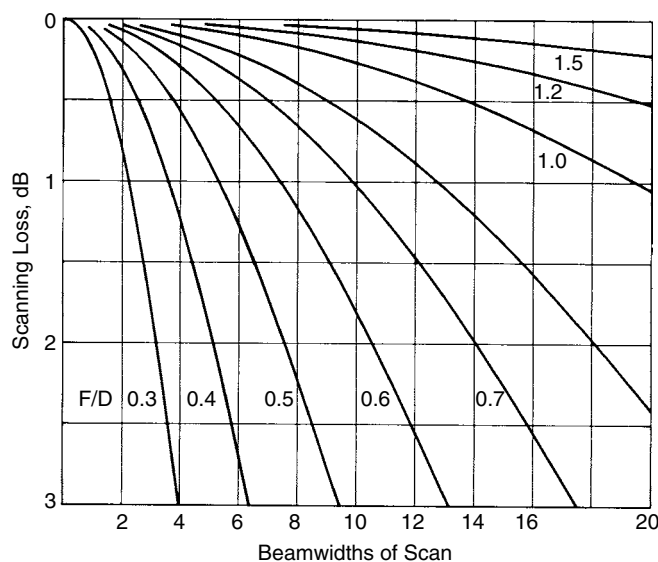


FIGURE 8-6 Feed-scanning loss of a paraboloidal reflector.

TABLE 8-2 Sidelobe Level of a Feed-Scanned Paraboloidal Reflector

Scanning Loss (dB)	Sidelobe Level (dB)	Scanning Loss (dB)	Sidelobe Level (dB)
0.50	14.1	1.75	10.1
0.75	12.9	2.0	9.7
1.00	11.9	2.5	9.0
1.25	11.2	3.0	8.5
1.50	10.6		

Example A reflector with a 50λ diameter is feed-scanned to 6° . Compute the offset distance and scanning loss when $f/D = 0.6$.

Use the approximation $\text{HPBW} = 70^\circ\lambda/D = 1.4^\circ$. The reflector is scanned $6/1.4 = 4.3$ beamwidths:

scanning loss (Figure 8-6) = 0.4 dB

sidelobe level (Table 8-2) = 14.6 dB

The angle between the axis and the feed point to vertex must be greater than the scan angle, since the reflector is concave:

$$\psi_s = \frac{\theta_s}{\text{BDF}} = \frac{6^\circ}{0.908} = 6.61^\circ \quad (\text{Table 8-1})$$

The offset distance is $f \tan 6.61^\circ = 0.6(50\lambda) \tan 6.61^\circ = 3.48\lambda$.

The scalar analysis of this section gives only approximate results. Large feed scanning produces higher-order aberrations other than coma [13–15]. The optimum gain point moves off the focal plane but fails to follow the curve predicted from optics for reflectors extremely large in wavelengths [14]. The reflector f/D and illumination taper determine the maximum gain contour for feed-scanning a reflector. Vector analysis improves the match between calculated and measured results [15].

8-7 RANDOM PHASE ERRORS

Reflector anomalies reduce the gain predicted from the feed analysis. We must specify reasonable manufacturing tolerances for the frequency of operation. It would appear that gain can be increased without bound by increasing the reflector diameter, but the tolerance problems of large reflectors limit the maximum gain. We consider only surface anomalies so small that on average the reflector retains its basic shape. The surface imperfections change the optical path length from the feed to the reflector aperture plane by $\delta(r, \phi)$, which gives us

$$\text{PEL} = \frac{\left| \int_0^{2\pi} \int_0^a E(r, \phi) e^{j\delta(r, \phi)} r dr d\phi \right|^2}{\left[\int_0^{2\pi} \int_0^a |E(r, \phi)| r dr d\phi \right]^2} \quad (8-17)$$

Cheng [16] bounds the phase error loss by using a limit on the integrals. Given a peak phase error of m (radians), the change in gain is bounded:

$$\frac{G}{G_0} \geq \left(1 - \frac{m^2}{2} \right)^2 \quad (8-18)$$

This gain loss estimate is too conservative, but it is useful as an upper bound.

Ruze [17] improved the random surface error loss estimate by using a Gaussian distributed error correlated over regions. Dents or segments making up the reflector are correlated with the errors over a nearby region. The error at a point depends on the location of nearby points in the correlation region. The phase error efficiency becomes an infinite series:

$$\text{PEL} = \exp(-\bar{\delta}^2) + \frac{1}{\eta} \left(\frac{2C}{D} \right)^2 \exp(-\bar{\delta}^2) \sum_{n=1}^{\infty} \frac{(\bar{\delta}^2)^n}{n \cdot n!} \quad (8-19)$$

where C is the correlation distance, D the diameter, and η the aperture efficiency (ATL). $\bar{\delta}^2$ is the mean-square phase deviation, given by

$$\bar{\delta}^2 = \frac{\int_0^{2\pi} \int_0^a |E(r, \phi)| \delta^2(r, \phi) r dr d\phi}{\int_0^{2\pi} \int_0^a |E(r, \phi)| r dr d\phi} \quad (8-20)$$

If we include the correlation distance, PEL decreases. The infinite series [Eq. (8-19)] converges rapidly. When the correlation distance is small compared with the diameter, the phase error efficiency becomes

$$\text{PEL} = \exp\left(\frac{-4\pi\epsilon_0}{\lambda}\right)^2 = \exp(-\bar{\delta}^2) \quad (8-21)$$

where ϵ_0 is the effective reflector tolerance. We use 4π instead of 2π because the wave travels to and from the reflector and the phase distance is twice the reflector tolerance. From Eq. (8-20) we derive the effective RMS tolerance:

$$\epsilon_o^2 = \frac{\int_0^{2\pi} \int_0^a |E(r, \phi)| \epsilon^2(r, \phi) r dr d\phi}{\int_0^{2\pi} \int_0^a |E(r, \phi)| r dr d\phi} \quad (8-22)$$

Ruze gives the distance ϵ in terms of the z -axis deviation Δz and the surface normal

$$\epsilon = \frac{\Delta z}{1 + (r/2f)^2} \quad \epsilon = \frac{\Delta n}{\sqrt{1 + (r/2f)^2}} \quad (8-23)$$

We evaluate the constants in Eq. (8-21) and convert to a decibel ratio:

$$\text{PEL(dB)} = -685.8 \left(\frac{\epsilon_0}{\lambda}\right)^2 \quad (8-24)$$

Example Compute the required reflector tolerance at 30 GHz to limit the RMS surface tolerance phase error loss to 1 dB.

Using Eq. (8-24), we get

$$\frac{\epsilon_0}{\lambda} = \sqrt{\frac{1}{685.8}} = 0.038$$

At 30 GHz, $\lambda = 1$ cm and $\epsilon_0 = 0.38$ mm. We can also use Eq. (8-18), which gives the upper bound on surface error loss:

$$m = \frac{4\pi\epsilon_0}{\lambda} = \sqrt{2 \left(1 - \sqrt{\frac{G}{G_0}}\right)} = 0.466 \text{ at } 1 \text{ dB}$$

$\epsilon_0 = 0.037\lambda$ or $\epsilon_0 = 0.37$ mm at 30 GHz. Both methods give about the same answer in this case.

Zarghamee [18] extended tolerance theory to include the effects of the surface error distribution. Some antennas have better support and construction in some areas and are more accurate in those areas. This improves the reflector performance. Zarghamee defined a second variation of surface deviations by

$$\eta_0^4 = \frac{\int_0^{2\pi} \int_0^a |E(r, \phi)| [\epsilon^2(r, \phi) - \epsilon_0^2] r dr d\phi}{\int_0^{2\pi} \int_0^a |E(r, \phi)| r dr d\phi}$$

The phase error efficiency becomes

$$\text{PEL} = \exp\left(\frac{-4\pi\epsilon_0}{\lambda}\right)^2 \exp\left(\frac{\pi\eta_0}{\lambda}\right)^4$$

The correlation of random errors increases the probable sidelobe level. The sidelobe level increases with the size of the correlation interval and decreases for larger aperture diameters. Increasing the amplitude taper of the distribution makes the aperture pattern more susceptible to random-error sidelobes, since increasing the taper is somewhat equivalent to decreasing the aperture diameter. Blockage and feed diffraction also limit the achievable sidelobe level in a reflector. A simple feed cannot carefully control the aperture distribution necessary for low sidelobes. Hansen [19, p. 74] discusses sidelobe limitations caused by random phase error in some detail.

Paraboloidal reflectors can be made in an umbrella shape where the ribs are parabolic and wire mesh is stretched between them [20]. The gore shape causes phase error loss and their periodicity produces extra sidelobes. Given the number of gores N_G and the focal length of the ribs f_r , the surface is given by

$$f(\psi) = f_r \frac{\cos^2(\pi/N_G)}{\cos^2 \psi}$$

where ψ is measured from the centerline between the ribs. We calculate the average focal length by integrating across the gore half-angle π/N_G and dividing by π/N_G :

$$f_{\text{av}} = f_r \frac{\sin(2\pi/N_G)}{2\pi/N_G} \quad (8-25)$$

We use Eq. (8-25) to calculate the rib focal length given the average focal length of the reflector.

The peak sidelobe due to the periodic gores occurs at an angle θ_p found from the number of gores and the diameter D :

$$\theta_p = \sin^{-1} \left(1.2 N_G \frac{\lambda}{\pi D} \right) \quad (8-26)$$

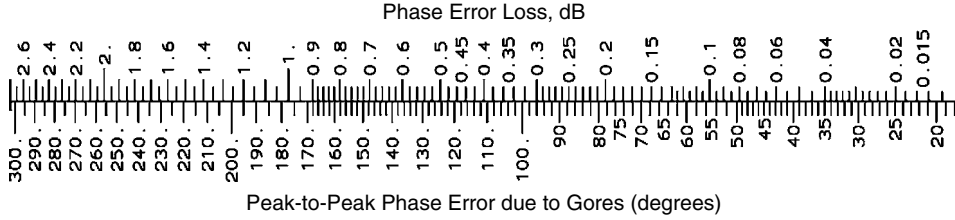
Given the average f/D of the reflector, we determine the peak-to-peak phase deviation across the gore by the approximate equation

$$\Delta = \frac{800 - 500(f/D - 0.4)}{N_G^2} \frac{D}{\lambda} \quad (8-27)$$

Scale 8-7 lists the phase error loss for a feed edge taper of 10 dB. Increasing the feed taper decreases the phase error loss due to gore construction. When we use a 20-dB feed taper, the values given by Scale 8-7 reduce by 0.16 dB for 0.5 dB of loss, 0.31 dB for 1 dB, and 0.45 dB for 1.5 dB. The gain losses due to underillumination by the 20-dB edge taper feed exceed these values.

Example Given a reflector with $D/\lambda = 35$ with a limit of 0.5 dB loss due to gore construction for $f/D = 0.34$, we discover that the allowable peak-to-peak phase error from Scale 8-7 is 124° . Using Eq. (8-27), we solve for the number of ribs:

$$N_G^2 = \frac{830}{124} 35 = 234 \quad \text{or} \quad N_G = 16$$



SCALE 8-7 Phase error loss due to gore construction of a paraboloidal reflector.

We use Eq. (8-26) to compute the angle of the peak gore sidelobe, $\theta_p = 10.0^\circ$. Equation (8-27) shows that the phase deviation Δ is proportional to frequency. If the frequency increases by 1.5 times, then by Eq. (8-27), 124° increases to 186° and we read 1.1 dB of loss from Scale 8-7 while the peak gore sidelobe becomes $\theta_p = 6.7^\circ$.

8-8 FOCAL PLANE FIELDS

We improve the efficiency and pattern response of a reflector if we match the feed fields to the focal plane fields. GO assumes a point focus, but an actual focus is extended. We determine the reflector and feed efficiency from the field match over the focal plane. When the reflector f/D value is large, we use the diffraction pattern of a circular aperture, the Airy function:

$$E = \frac{J_1(kr\psi_0)}{kr\psi_0} \quad (8-28)$$

where ψ_0 is the half subtended angle of the reflector (radians), r the radial coordinate, k the propagation constant, and J_1 the Bessel function.

In a more exact method the currents induced on the reflector ($2\mathbf{n} \times \mathbf{H}$) and the magnetic vector potential are used to calculate the focal plane fields. As f/D decreases, the currents on the reflector interact and modify their distribution, but it is a secondary effect [21]. Iterative physical optics analysis (section 2-4) can find these current modifications. We calculate the reflector efficiency from the field match of the focal plane fields ($\mathbf{E}_1, \mathbf{H}_1$) and the fields of the feed ($\mathbf{E}_2, \mathbf{H}_2$) using Robieux's theorem [4]:

$$\eta = \frac{\left| \iint_S (\mathbf{E}_1 \times \mathbf{H}_2 - \mathbf{E}_2 \times \mathbf{H}_1) \cdot d\mathbf{S} \right|^2}{4P_1 P_2} \quad (8-29)$$

where P_1 and P_2 are the input powers to produce the fields and η is the efficiency. Equation (8-29) is the magnitude squared of Eq. (2-35), the reactance equation equivalence applied to Eq. (1-55) for the coupling between two antennas S_{21} . The finite size of the feed causes spillover. The extent of amplitude and phase mismatch between the two fields determines the efficiency. By illuminating the reflector with a cross-polarized wave, we compute the cross-polarization radiation level through its field match [Eq. (8-29)].

We maximize efficiency [Eq. (8-29)] by conjugate-matching the focal plane fields with the feed fields. Corrugated horns can be designed by expanding the focal plane

fields in axial hybrid modes of the horn and mode matching [22,23]. Wood [4] expands the reflector and feed fields in spherical harmonics and matches them at a boundary. Both sets of fields can be approximated very well by just a few terms, and this method can handle dual-reflector and offset reflector systems as well as axisymmetric prime focus reflectors.

We can feed the reflector with an array to match the focal plane fields [24–26]. The array samples the focal plane field and conjugate-matches it so that the powers sum in phase. The array can form multiple beams and also correct reflector aberrations [24]. By using the multiple feeds of the array, coma can be reduced for scanned beams and efficiency improved. However, quantization of the array element locations and excitations, amplitude, and phase reduces efficiency and raises the sidelobe level [27].

We apply Eq. (1-55) for the coupling between two antennas to determine the feeding coefficients of an array feed for a dish. Assume an incident field distribution on the reflector that includes the incident wave direction and the desired aperture distribution for the reflector. Using physical optics, we calculate the currents induced on the reflector surface. If the reflector has significant curvature so that the patches face each other, iterative PO can be used to account for their interaction. We calculate the fields radiated by each feed on the reflector surface and apply Eq. (1-55) to calculate coupling. This method applies the feed pattern to the calculation instead of the point matching used in a focal plane solution. Similar to scanning of an array, we use conjugative matching for the feed array elements to produce the beam desired. This method can determine array feed element amplitude and phase for any composite reflector aperture distribution that includes aperture distribution to control sidelobes or include multiple beams. The method reduces coma to the minimum possible with a given array.

Analysis finds the array distribution desired, but we do not achieve this distribution merely by designing the feed network to produce these amplitudes and phases because the feed elements have significant mutual coupling. We need to include the effect of the paraboloidal reflector when computing mutual coupling because the field radiated by one feed induces currents on the reflector that couple to other feed elements. Below we show that the effect of the reflector diminishes as the reflector diameter increases. If the mutual coupling is significant whether direct or due to the reflector, we need to apply the corrections given in Section 3-11 to adjust the feeding coefficients of the array.

8-9 FEED MISMATCH DUE TO THE REFLECTOR

The feed receives some of its transmitted power because it reflects from the parabola and returns as a mismatch at the feed terminals. We calculate the reflected field at the feed by using surface currents and the magnetic vector potential. The only significant contribution comes from areas near where the normal of the reflector points at the feed. Around every other point, the phase of the reflection varies rapidly and cancels and we need to consider only points of stationary phase. We calculate the reflection from each point of stationary phase from [2]

$$\Gamma = -j \frac{G_f(\rho_0)}{4k\rho_0} \sqrt{\frac{\rho_1\rho_2}{(\rho_1 + \rho_0)(\rho_2 + \rho_0)}} e^{-j2k\rho_0} \quad (8-30)$$

where Γ is the reflection coefficient, ρ_0 the distance to the stationary phase point, $G_f(\rho_0)$ the feed gain in the direction of ρ_0 , and ρ_1 and ρ_2 the radiuses of curvature of the reflector at ρ_0 . The vertex is the only point of stationary phase on a paraboloidal reflector: $\rho_1 = \rho_2 = -2f$ and $\rho_0 = f$. Equation (8-30) reduces to

$$\Gamma = -j \frac{G_f(0)}{2kf} e^{-j2kf} \quad (8-31)$$

Example Suppose that we have a reflector with $f/D = 0.40$. Compute reflector mismatch for a source with its 10-dB beamwidth equal to the reflector subtended angle.

Half subtended angle [Eq. (8-2)] $\psi_0 = 2 \tan(1/1.6) = 64^\circ$. By using the feed approximation $\cos^{2N}(\theta/2)$, we have

$$N = \frac{\log 0.1}{2 \log \cos(64^\circ/2)} = 6.98$$

The feed gain at the boresight is $N + 1$ [Eq. (1-20c)]:

$$[\text{Eq. (8-31)}] \quad |\Gamma| = \frac{8\lambda}{4\pi f} = 1.59 \frac{\lambda}{D}$$

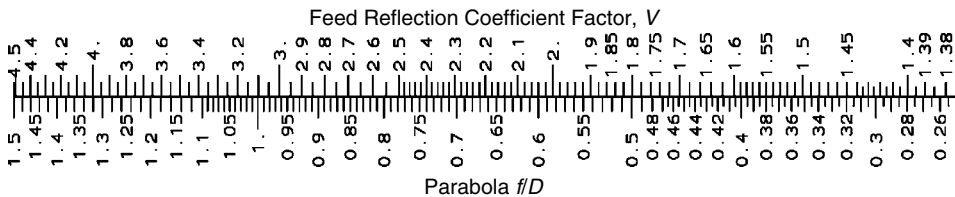
Increasing the reflector diameter in wavelengths decreases the reaction of the reflector on the feed. For example, given a 3-m reflector at 4 GHz, we calculate reflector reflection coefficient as 0.04, or VSWR = 1.08.

We can express the reflector reflection of a paraboloidal reflector as

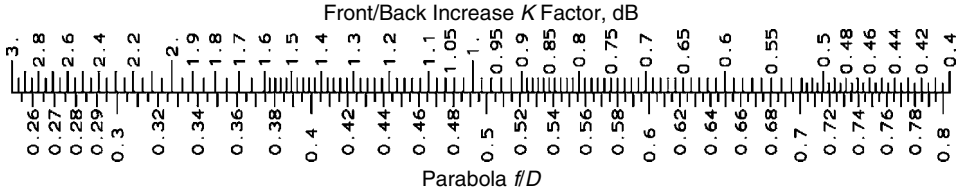
$$|\Gamma| = V \frac{\lambda}{D} \quad (8-32)$$

and calculate Scale 8-8 of V versus f/D for feeds with 10-dB beamwidths equal to the reflector subtended angle. Higher reflector f/D values produce larger feed reflections, since the feed gain increases faster than the reduced area of the reflector seen from the feed.

Narrowband corrections to these reflections can be designed by using a vertex plate (Silver [2]) or by designing sets of concentric ring ridges in the reflector (Wood [4]). The rings can match the feed at more than one frequency. By any of these methods, the free-space mismatch of the feed could be corrected for, but, of course, the feed itself can be mismatched to compensate for the reflector reaction.



SCALE 8-8 Feed reflection scale factor V given f/D .



SCALE 8-9 Paraboloidal reflector front-to-back ratio increase K given f/D .

8-10 FRONT-TO-BACK RATIO

Figure 2-9 illustrates the pattern response of a paraboloidal reflector and shows that the pattern behind the reflector peaks along the axis. The diffractions from all points along the rim add in-phase along the axis and produce a pattern peak. We can reduce this rim diffraction by using a rolled, serrated, or castellated edge to reduce diffraction. An absorber-lined cylindrical shroud extending out to enclose the feed will greatly reduce back radiation, including spillover, and allows the close spacing of terrestrial microwave antennas with reduced crosstalk.

For a normal truncated circular reflector rim, the following equation estimates the front-to-back ratio given the reflector gain G , the feed taper T , and feed gain G_f [28]:

$$F/B = G + T + K - G_f \quad \text{dB} \quad (8-33)$$

The constant K , given by Scale 8-9, is related to f/D :

$$K = 10 \log \left[1 + \frac{1}{(4f/D)^2} \right] \quad (8-34)$$

Example Estimate F/B for a reflector with $f/D = 0.34$ and 40 dB of gain.

We read the feed subtended angle from Scale 8-1 to be 143° . A 10-dB edge taper feed has a gain of about 8.1, found from Scale 1-2. Using Eq. (8-33), we estimate $F/B = 40 + 10 + 1.9 - 8.1 = 43.8$ dB.

8-11 OFFSET-FED REFLECTOR

Moving the feed out of the aperture eliminates some of the problems with axisymmetrical reflectors. Blockage losses and diffraction-caused sidelobes and cross-polarization disappear. We can increase the size of the feed structure and include more if not all of the receiver with the feed. For example, the reflector may be deployed from a satellite, with the feed mounted on the main satellite body.

Figure 8-7 shows the offset-fed reflector geometry. We form the reflector out of a piece of a larger paraboloid. Every piece of the paraboloidal reflector converts spherical waves from the focus into a plane wave moving parallel with its axis. We point the feed toward the center of the reflector to reduce the spillover, but we still locate the feed phase center at the focus of the reflector. The aperture plane projects to a circle, although the rim shape is an ellipse. ψ_0 is the angle from the axis of the parabola to

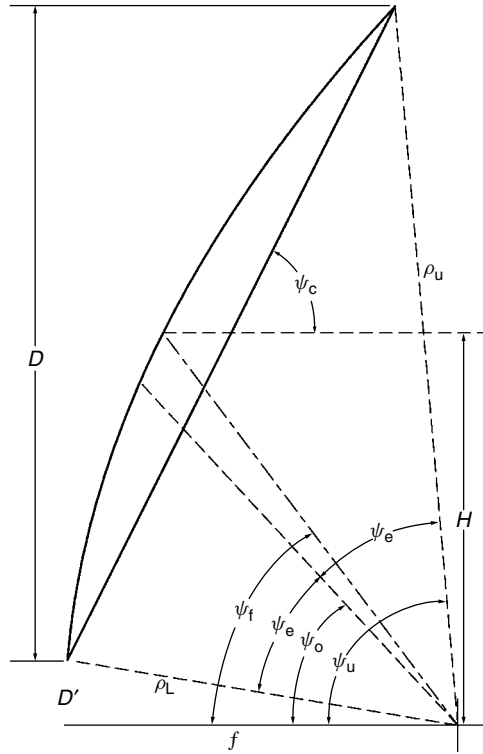


FIGURE 8-7 Parameters of an offset-fed parabolic reflector.

the center of the cone of the reflector, and the reflector subtends an angle $2\psi_e$ about this centerline. Given the aperture plane diameter D and the height H of the center, we find the lower rim offset $D' = H - D/2$. From these parameters we determine the angle of the center of the rim cone from the z -axis:

$$\psi_0 = \tan^{-1} \frac{16fH}{16f^2 + D^2 - 4H^2} = \tan^{-1} \frac{2f(D + 2D')}{4f^2 - D'(D + D')} \quad (8-35)$$

The half cone angle defines the rim:

$$\psi_e = \tan^{-1} \frac{8fD}{16f^2 + 4H^2 - D^2} = \tan^{-1} \frac{2fD}{4f^2 + D'(D + D')} \quad (8-36)$$

We direct the feed an angle ψ_f from the z -axis to the center of the projected diameter different from the angle ψ_0 of the rim cone axis:

$$\psi_f = 2 \tan^{-1} \frac{H}{2f} = 2 \tan^{-1} \frac{2D' + D}{4f} \quad (8-37)$$

The rim lies in a plane at an angle ψ_c with respect to the z -axis:

$$\psi_c = \tan^{-1} \frac{2f}{H} = \tan^{-1} \frac{4f}{2D' + D} \quad (8-38)$$

The rim is an ellipse in this plane with major and minor axes given by

$$a_e = \frac{D}{2 \sin \psi_c} \quad \text{and} \quad b_e = \frac{D}{2} \quad (8-39)$$

The offset angle modifies the f/D of the reflector:

$$\frac{f}{D} = \frac{\cos \psi_e + \cos \psi_0}{4 \sin \psi_e} \quad (8-40)$$

We calculate the rim offset from the cone angles:

$$D' = 2f \tan \frac{\psi_0 - \psi_e}{2} \quad (8-41)$$

Manufacturing an offset reflector requires specification of the reflector when laid on its rim in the x - y plane so that the mold can be machined. We center the major axis of the reflector elliptical rim $L = 2a_e$ along the x -axis and the minor axis D along the y -axis. In this position the reflector depth $d(x, y)$ is found from the expression [29]

$$d(x, y) = \frac{2fL^3}{D(L^2 - D^2)} \left[\sqrt{1 + \frac{x D^2 \sqrt{L^2 - D^2}}{fL^3} + \frac{D^2(L^2 - D^2)}{4f^2L^4} \left(\frac{D^2}{4} - y^2 \right)} - 1 - \frac{x D^2 \sqrt{L^2 - D^2}}{2fL^3} \right] \quad (8-42)$$

The deepest point of the reflector d_{\max} occurs along the x -axis at x_b :

$$x_b = -\frac{D^2 \sqrt{L^2 - D^2}}{16fL} \quad \text{where} \quad d_{\max} = \frac{D^3}{16fL} \quad (8-43)$$

After measuring D , L , and d_{\max} , we determine the offset focal length from the equation

$$f = \frac{D^3}{16Ld_{\max}} \quad (8-44)$$

We calculate the center height of the offset from

$$H = 2f \sqrt{\frac{L^2}{D^2} - 1} \quad (8-45)$$

We calculate the reflector half cone angle ψ_e and the cone axis angle from the z -axis and ψ_0 from the focal length f , ellipse major diameter L , and minor diameter D :

$$\begin{bmatrix} \psi_e \\ \psi_0 \end{bmatrix} = \tan^{-1} \left(\sqrt{\frac{L^2}{D^2} - 1} + \frac{D}{4f} \right) \mp \tan^{-1} \left(\sqrt{\frac{L^2}{D^2} - 1} - \frac{D}{4f} \right) \quad (8-46)$$

To align the reflector, we use the angle of the reflector rim major axis $\psi_c = \sin^{-1}(D/L)$ with respect to the z -axis and the radial distances from the lower and upper edges of the reflector in the offset plane, since the center offset H is not a distinguishable point:

$$\begin{bmatrix} \rho_U \\ \rho_L \end{bmatrix} = \frac{fL^2}{D^2} + \frac{D^2}{16f} \pm D \left(\frac{L^2}{D^2} - 1 \right) \quad (8-47)$$

We analyze the offset reflector with the same tools as those used with the axisymmetric reflector: aperture field, physical optics, and GTD. The asymmetry of the reflector to feed geometry introduces anomalies. Huygens sources no longer eliminate cross-polarization, because the source must be tilted. Symmetry prevents cross-polarization in the plane containing the x -axis (Figure 8-8), but cross-polarization for linear polarization increases in the plane containing the y -axis (symmetry plane) as f/D decreases

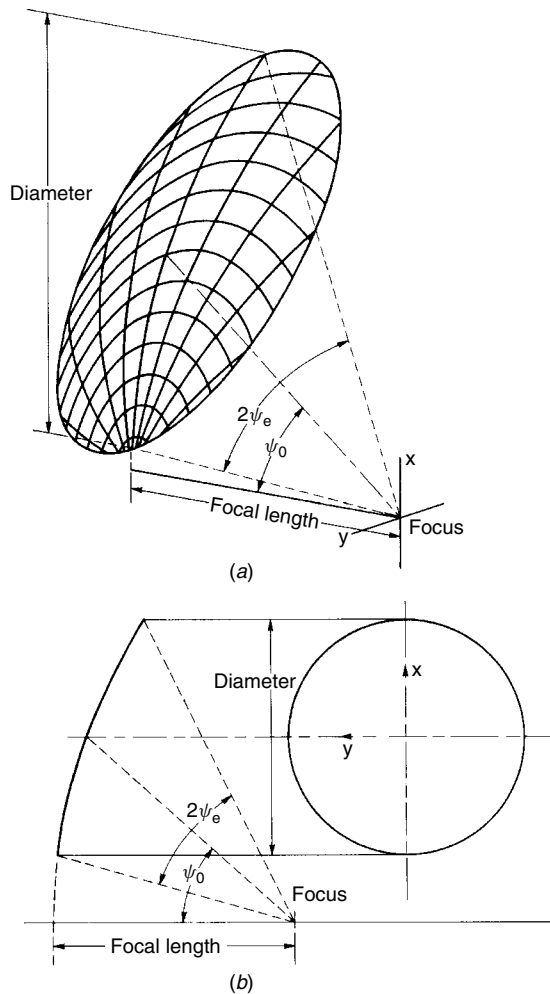


FIGURE 8-8 Offset-fed paraboloidal reflector geometry: (a) perspective; (b) orthographic representation.

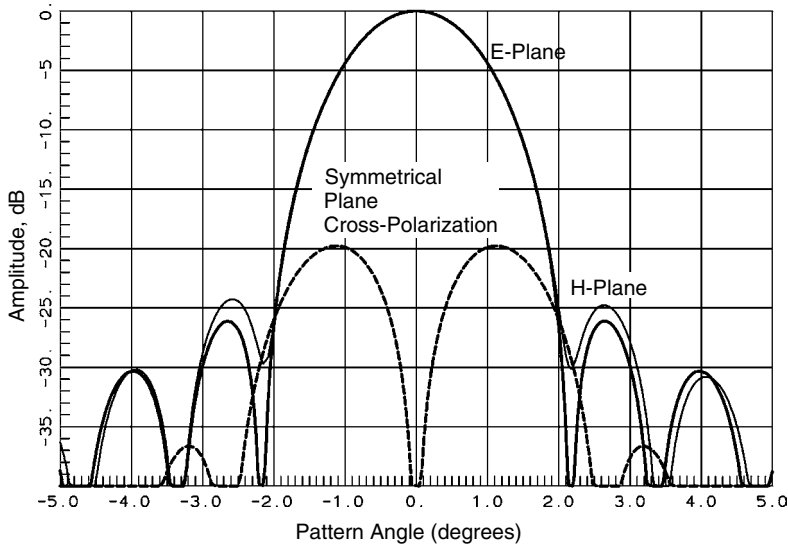


FIGURE 8-9 Pattern of an offset-fed reflector with linearly polarized feed.

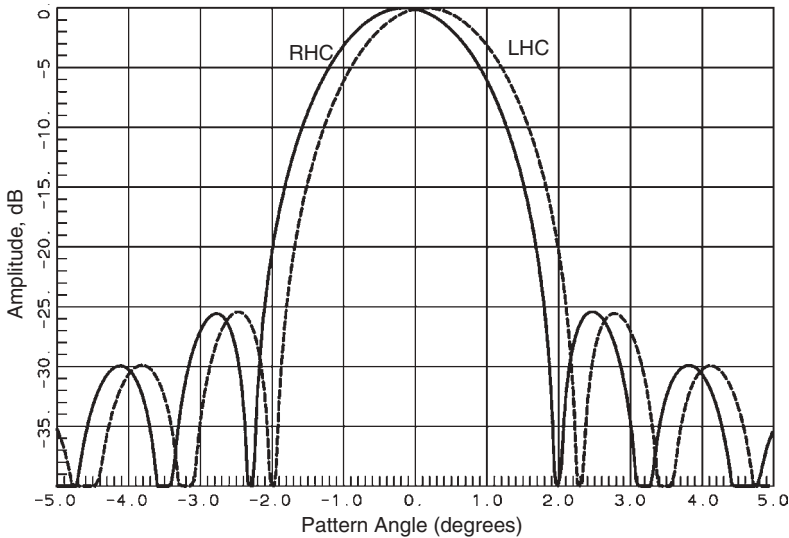


FIGURE 8-10 Pattern of an offset-fed reflector with circularly polarized feed.

(Figure 8-9). The Condon lobes move off the diagonal planes and into the plane containing the y -axis. The asymmetry along the x -axis tapers the amplitude distribution from a symmetrical feed, since the spherical wave travels farther to the outer edge of the reflector than to the lower edge. The offset-fed reflector geometry squints circularly polarized pattern peaks in the symmetrical (y -axis) plane without generating cross-polarization (Figure 8-10). An approximate formula for the squint is [9]

$$\psi_s = \sin^{-1} \frac{\lambda \sin \psi_0}{4\pi f} \quad (8-48)$$

where ψ_s is the squint angle. Opposite senses of circular polarization squint in opposite directions and cause a problem with dual circularly polarized feed systems. In all cases increasing the f/D or the effective f/D through a subreflector reduces these problems. The subreflector should be kept out of the aperture of the main reflector. We can feed-scan the offset-fed reflector by moving the feed laterally along a line that lies perpendicular to the boresight of the feed (the line defined by ψ_0). We must modify the beam deviation factor (BDF):

$$\text{BDF}_{\text{offset fed}} = \text{BDF}_{\text{center fed}} \frac{(f/D)_{\text{offset}}}{(f/D)_{\text{center fed}}} \quad (8-49)$$

Example Given an offset-fed reflector with $\psi_0 = 45^\circ$ and $\psi_e = 40^\circ$, compute the beam deviation factor.

From Eq. (8-49),

$$\begin{aligned} \left(\frac{f}{D}\right)_{\text{center fed}} &= \frac{\cos 40^\circ + 1}{4 \sin 40^\circ} = 0.687 \\ \left(\frac{f}{D}\right)_{\text{offset fed}} &= \frac{\cos 40^\circ + \cos 45^\circ}{4 \sin 40^\circ} = 0.573 \end{aligned}$$

From Table 8-1 we interpolate $\text{BDF}_{\text{center fed}} = 0.928$, and we substitute the values into Eq. (8-49) to calculate $\text{BDF}_{\text{offset fed}} = 0.774$. We must laterally offset the feed farther than with a center-fed reflector to achieve the same feed scanning.

Periscope Configuration The periscope consists of an offset paraboloidal reflector with $\psi_0 = 90^\circ$ with a long focal length fed by a paraboloidal reflector located at the focus. This eliminates the need to run a transmission line up a tower. Periscope antennas can be made using a flat-plate reflector, but the long focal length means that the parabolic splash plate antenna has only a small deviation from flat. The flat plate is limited to a gain of only 6 dB more than the feed reflector for optimum conditions with a large plate. The gain of the offset paraboloidal reflector is determined by the diameter of the splash plate, not the feed reflector. Because the splash plate is in the near field of the feeding reflector, gain is reduced by phase error, whereas spillover and amplitude taper losses also contribute to gain loss.

Design starts with determining the splash reflector center height H required to clear obstacles along the transmission path. We calculate the splash reflector aperture diameter from the required gain and beamwidth. The periscope configuration contributes to gain loss, but with proper selection of the feed paraboloidal reflector these losses are minor and can be compensated for by using a larger splash reflector. Having the splash reflector directly overhead corresponds to a parent reflector design with $f/D_p = 0.25$ and $f = H/2$. An analysis using a radial parabolic aperture distribution in the feed reflector determined that the optimum feed reflector diameter is found from the ratio of height to projected splash reflector aperture diameter D_s [30]:

$$D_f = \frac{2\lambda H}{D_s} = \frac{\alpha\lambda H}{D_s} \quad \text{or} \quad \alpha = \frac{D_s D_f}{\lambda H} = \frac{D_s D_f F}{H c} \quad (8-50)$$

Whereas $\alpha = 2$ is the optimum dimensions at a particular frequency, we account for shift from the optimum with this factor. The parameter α is the frequency response

factor for frequency F and speed of light c . The illumination efficiency is the product of the feed reflector illumination efficiency and the periscope efficiency factor η_p :

$$\eta_p = \frac{4 [1 - (1 - K)J_0(m) - K(2/m)J_1(m)]}{m^2(1 - K/2)^2} \quad (8-51)$$

J_0 and J_1 are Bessel functions, $m = \alpha\pi/2$, and $K = 1 - 10^{-[\text{ET}(\text{dB})/20]}$ for the feed reflector edge illumination taper $\text{ET}(\text{dB})$. Table 8-3 lists the added illumination loss of a periscope, given geometry using α in Eq. (8-50) for a 12-dB edge taper in a feeding reflector.

Example A periscope antenna system placed a 3-m projected aperture splash reflector 30 m above the feed reflector to operate at 12 GHz ($\lambda = 0.05$ m). Using Eq. (8-50), we calculate the feed reflector diameter to be 0.5 m for $\alpha = 2$. If we assume that the feed reflector has an efficiency of 60% (-2.22 dB), the efficiency of the splash reflector will be -2.6 dB:

$$\text{gain (dB)} = 20 \log \frac{\pi D_s}{\lambda} - 2.6 = 20 \log \frac{3\pi}{0.05} - 2.6 = 42.9$$

The focal length f of the splash reflector is $H/2 = 15$ m. Since the angle of the splash reflector rim is 45° , $L = D_s / \sin(45^\circ) = 4.24$ m. We determine the maximum depth of the reflector by using Eq. (8-43) to be 2.65 cm located 2.65 cm off center. The splash reflector increased the gain relative to the feed reflector by 7.4 dB.

8-12 REFLECTIONS FROM CONIC SECTIONS

We use reflectors made from conic sections other than the parabola as subreflectors. The ellipse and hyperbola rotated about their axes to form solid figures that reflect incident spherical waves into spherical waves with different caustics (focal points). Reflectors formed by moving the figure along a line change the caustics of cylindrical waves. We consider only spherical waves, but we need only convert to cylindrical waves for cylindrical reflectors.

All conic-section reflectors convert spherical waves from one focus into spherical waves directed toward the other focus. The ellipse has its two focuses located within the

TABLE 8-3 Added Illumination Loss of a Periscope, Given Geometry Using α in Eq. (8-50) for 12-dB Edge Taper in a Feeding Reflector (dB)

α	η_p	α	η_p
1.0	3.17	2.2	0.45
1.2	2.06	2.4	0.68
1.4	1.28	2.6	1.04
1.6	0.77	2.8	1.52
1.8	0.48	3.0	2.11
2.0	0.38	3.2	2.79
		3.4	3.53

figure. As we let one focus approach infinity, the ellipse transforms into a parabola. If the focus is pushed through infinity to the negative axis, the figure becomes a hyperbola located between the two foci. Figure 8-11 shows the ray tracing for axisymmetrical conic section reflectors. A spherical source at one focus is reflected to the second focus by the reflector, although it is virtual (not actually reached) in some cases.

We describe all conic sections with the same polar equation:

$$\rho = \frac{eP}{1 - e \cos \theta} \quad (8-52)$$

where P is the distance between the origin, the focus, to a line called the *directrix* (Figure 8-12). The eccentricity e is the ratio of the distance from the origin to a point on the curve to the distance from the same point to the directrix: $r_1 = er_2$. In an ellipse, $e < 1$; in a parabola, $e = 1$; and in a hyperbola, $e > 1$. The distance between the foci is

$$2c = \frac{2Pe^2}{1 - e^2} \quad (8-53)$$

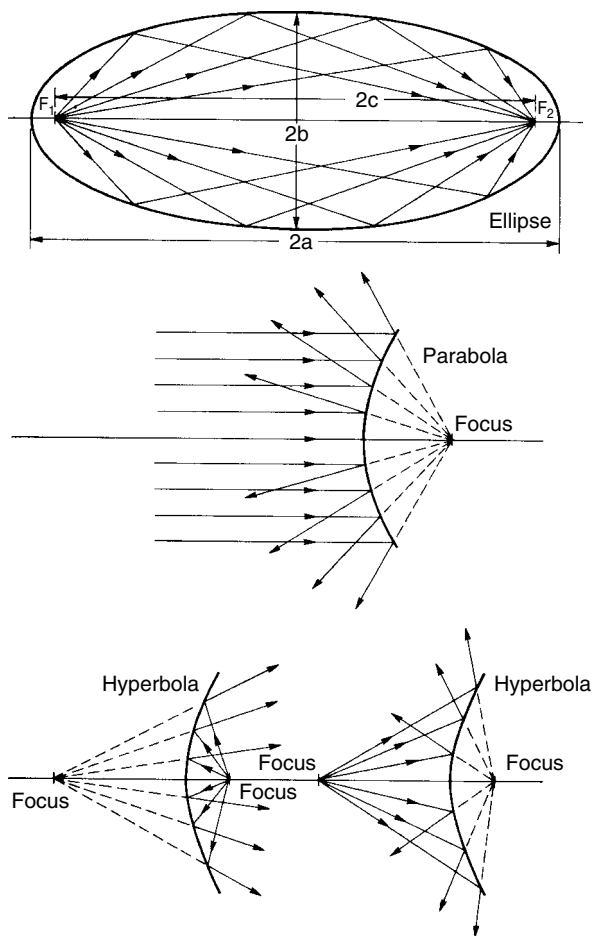


FIGURE 8-11 Reflections from conic-section reflectors.

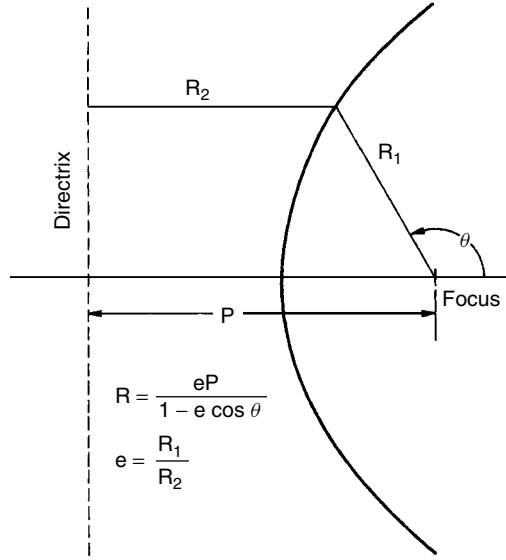


FIGURE 8-12 Conic-section geometry.

A hyperbola with its axis containing the two foci along the z -axis, located at $\pm c$, intersects the z -axis at $\pm a$ and satisfies the equation

$$\frac{z^2}{a^2} - \frac{r^2}{b^2} = 1 \quad \text{where} \quad b^2 = c^2 - a^2 \quad \text{and} \quad e = \frac{c}{a} > 1 \quad (8-54)$$

When we take the portion of the hyperbola along the $+z$ -axis that intersects the axis at $+a$, we define the angles from the two foci from the line between them because we place the feed at the left focus and locate a parabola focus at the right hyperbola focus. The left angle θ is the feed angle, and the right angle ψ is the parabola angle in a dual-reflector antenna. Given a point on the hyperbola, the distance from the left focus is ρ_1 and the distance from the right focus is ρ_2 :

$$\rho_1 = \frac{a(e^2 - 1)}{e \cos \theta - 1} = \frac{b^2}{e \cos \theta - 1} \quad \text{and} \quad \rho_2 = \frac{a(e^2 - 1)}{e \cos \psi + 1} = \frac{b^2}{e \cos \psi + 1} \quad (8-55)$$

We determine the radial position off the axis from either polar equation:

$$r = \rho_1 \sin \theta = \rho_2 \sin \psi \quad (8-56)$$

The two angles are related by the eccentricity e :

$$(e + 1) \tan \frac{\theta}{2} = (e - 1) \tan \frac{\psi}{2} \quad (8-57)$$

At a given point on the hyperbola, the angle of the normal u relative to the radial line ρ_1 is half the sum of the two angles, $u = (\theta + \psi)/2$. We need the radius of curvatures in the principal planes to apply Eq. (2-77) for reflection from a curved surface: R_1 in

the r - z plane and R_2 in the ϕ - z plane:

$$R_1 = \frac{b^2}{a \cos^2 u} \quad \text{and} \quad R_2 = \frac{b^2}{a \cos u} \quad (8-58)$$

When we offset-feed a hyperboloid, a cone determines the rim and it lies in a planar ellipse. Similar to the offset paraboloid, we center the cone at an angle θ_0 from the axis and define the cone by the half feed edge angle θ_e . We compute the distances from the focus to the upper and lower rim along the major axis of the rim ellipse:

$$\rho_L = \frac{b^2}{e \cos(\theta_0 - \theta_e) - 1} \quad \text{and} \quad \rho_U = \frac{b^2}{e \cos(\theta_0 + \theta_e) - 1}$$

We determine the major axis diameter ($2a_e$) of the elliptical rim from the triangle with sides ρ_L and ρ_U and angle $2\theta_e$ between them:

$$2a_e = \sqrt{\rho_L^2 + \rho_U^2 - 2\rho_L\rho_U \cos 2\theta_e} \quad (8-59)$$

The minor axis diameter ($2b_e$) is given by the equation

$$2b_e = \sqrt{(2a_e)^2 - (\rho_L - \rho_U)^2} \quad (8-60)$$

An ellipsoid can also be used as a subreflector in a dual-reflector antenna. Its equations are similar to the hyperboloid:

$$\frac{z^2}{a^2} + \frac{r^2}{b^2} = 1 \quad \text{and} \quad b^2 = a^2 - c^2 \quad \text{with} \quad e = \frac{c}{a} < 1 \quad (8-61)$$

We locate the ellipse with its major axis along the z -axis and use the portion that intersects the $+z$ -axis in a dual-reflector antenna. We place a feed at the left focus and the focal point of a paraboloid at the right ellipse focus. The radial distances to the two foci are given by the equations

$$\rho_1 = \frac{a(e^2 - 1)}{1 - e \cos \theta} = \frac{b^2}{1 - e \cos \theta} \quad \text{and} \quad \rho_2 = \frac{a(e^2 - 1)}{1 + e \cos \psi} = \frac{b^2}{1 + e \cos \psi} \quad (8-62)$$

The ellipse uses Eqs. (8-56) and (8-57) without change, but the angle of the normal u relative to the vector ρ_1 is the average difference between the two angles, $u = (\theta - \psi)/2$. Using the new angle u , Eq. (8-58) gives the principal radiuses of curvature at the point on an ellipsoid.

When we offset an ellipsoid by determining the rim as the intersection of an offset cone with it, we use the left equation of Eq. (8-62) for the upper and lower radiuses. The rim is a planar ellipse whose major and minor diameters are found using Eqs. (8-59) and (8-60), a consequence of Eq. (8-52) that defines both an ellipse and a hyperbola.

8-13 DUAL-REFLECTOR ANTENNAS

We derive dual-reflector antennas, Cassegrain and Gregorian, from their optical telescope counterparts. Each increases the effective focal length. In the Cassegrain dual-reflector antenna a hyperbolic subreflector is used (Figure 8-13), and in the Gregorian

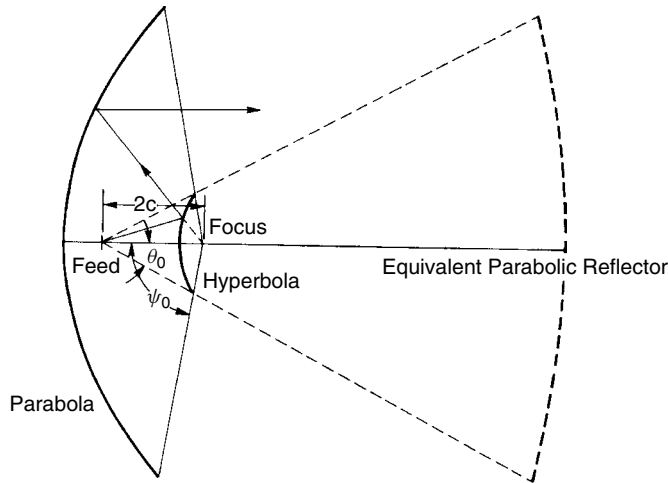


FIGURE 8-13 Cassegrain reflector antenna.

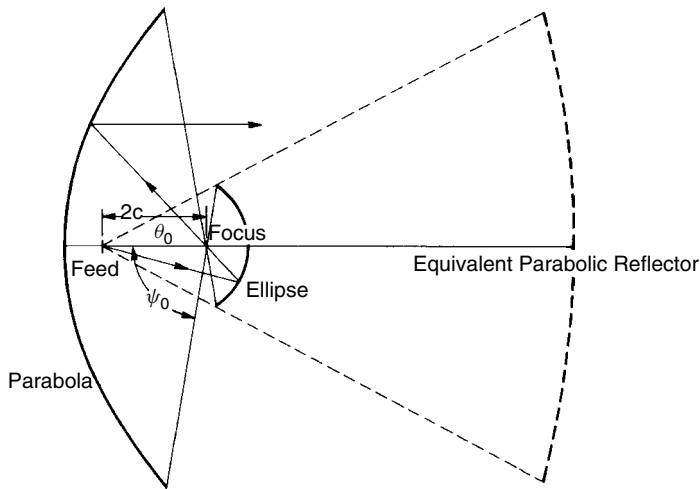


FIGURE 8-14 Gregorian reflector antenna.

dual-reflector antenna an elliptical subreflector is used (Figure 8-14). We locate one focus of the subreflector at the focus of the main paraboloidal reflector and place the second focus of the subreflector at the feed antenna phase center. The subreflector changes the curvature of waves coming from one focus into waves with their caustic at the second subreflector focus.

The number of Cassegrain designs exceeds the number of Gregorian dual reflectors. The Gregorian design requires a larger subreflector support because it extends farther from the main reflector vertex. The subreflector edge curvature increases the diffraction and reduces the control of the field incident on the main reflector, but by shaping the subreflector of the Cassegrain, we can increase overall efficiency. The inversion of the fields in the Gregorian reflector complicates such procedures.

In Figures 8-13 and 8-14 the subtended angle of the main reflector is $2\psi_0$, but the effective subtended angle at the feed is $2\theta_0$. We can calculate subreflector eccentricity from those angles.

$$\begin{array}{cc} \text{Cassegrain} & \text{Gregorian} \\ e = \frac{\sin \frac{1}{2}(\psi_0 + \theta_0)}{\sin \frac{1}{2}(\psi_0 - \theta_0)} & e = \frac{\sin \frac{1}{2}(\psi_0 - \theta_0)}{\sin \frac{1}{2}(\psi_0 + \theta_0)} \end{array} \quad (8-63)$$

We can analyze the dual-reflector system by using an equivalent parabola (Figures 8-13 and 8-14) from the subreflector subtended angle $2\theta_0$. We define the magnification factor as the ratio of the effective focal length to the actual focal length of the main reflector: $M = f_e/f$. The subreflector eccentricity can be calculated from M :

$$\begin{array}{cc} \text{Cassegrain} & \text{Gregorian} \\ e = \frac{M + 1}{M - 1} & e = \frac{M - 1}{M + 1} \end{array} \quad (8-64)$$

Equation (8-53) gives the distance between the focuses of the subreflectors:

$$\begin{array}{cc} \text{Cassegrain} & \text{Gregorian} \\ 2c = \frac{2Pe^2}{e^2 - 1} & 2c = \frac{2Pe^2}{1 - e^2} \end{array} \quad (8-65)$$

We gain the design parameter P and with it some freedom in the placement of the feed. We easily solve for the length P in terms of the distance between focuses $2c$:

$$\begin{array}{cc} \text{Cassegrain} & \text{Gregorian} \\ P = \frac{2c(e^2 - 1)}{2e^2} & P = \frac{2c(1 - e^2)}{2e^2} \end{array} \quad (8-66)$$

The subreflector diameter varies with P :

$$D_s = \frac{2eP \sin(\pi - \psi_0)}{1 - e \cos(\pi - \psi_0)} \quad (8-67)$$

We easily manipulate the geometry to find the distance from the main reflector vertex to the feed focus L_m and from the feed focus to the subreflector L_s for both the Cassegrain and Gregorian reflectors. $L_m = f - 2c$ and $L_s = a + c = c(1 + 1/e)$. Additional sets of equations are available to obtain the geometry of the dual reflector for various sets of specified input parameters [31].

8-13.1 Feed Blockage

The increased effective focal length requires feeds with narrow beamwidths, and we can no longer consider the feed as a point source. It projects a shadow into the center of the reflector (Figure 8-15) and causes a central blockage. The subreflector also blocks the center. As we reduce the subreflector diameter to reduce blockage, the feed antenna moves closer to the subreflector and its projected shadow increases. The optimum occurs when the projected feed blockage diameter equals the subreflector diameter.

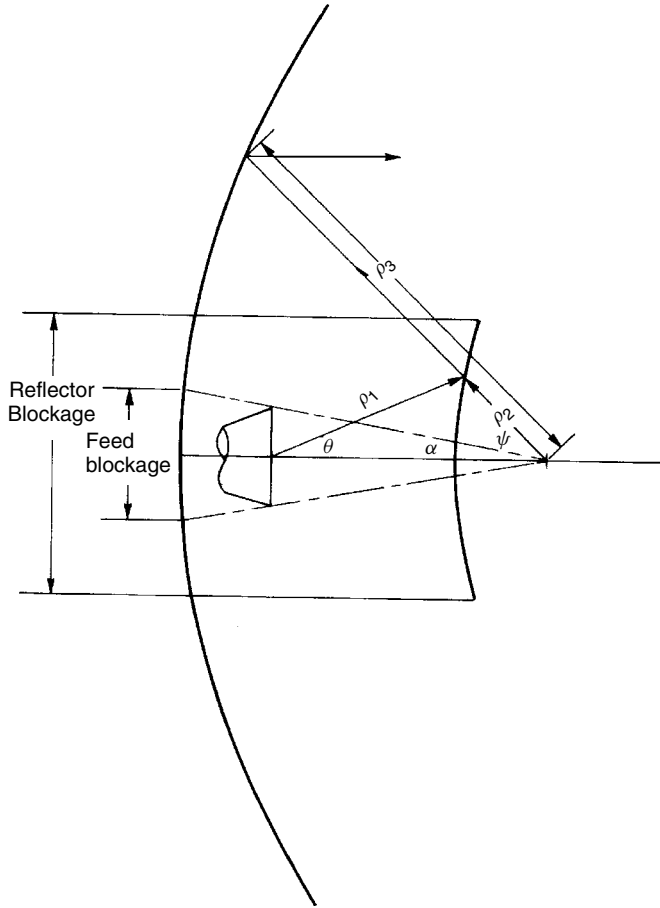


FIGURE 8-15 Cassegrain central blockage.

The feed size depends on the frequency of operation and the effective f/D value, whereas the subreflector diameter depends only on geometry. We cannot determine the optimum independent of frequency.

Example Design a 10-m-diameter main reflector Cassegrain antenna with $f/D = 0.3$ and an effective $f/D = 1.5$ to operate at 3.9 GHz. Minimize the aperture blockage.

$$M = \frac{1.5}{0.3} = 5 \quad [\text{Eq. (8-64)}] \quad e = \frac{5+1}{5-1} = 1.5$$

From Eq. (8-2),

$$\theta_0 = 2 \tan^{-1} \frac{1}{4(1.5)} = 18.9^\circ$$

We feed the reflector with a circular corrugated horn with a 10-dB beamwidth equal to the subtended angle of the subreflector. We use the methods of Section 7-3 to design the horn. When we include the thickness of the corrugations, we calculate a horn diameter

of 0.415 m. We determine the blockage angle α (Figure 8-15): $\alpha = \tan^{-1}(0.415/4c)$. From Eq. (8-56), $2c = 3.6P$. We use Eq. (8-67) with the parabola P_0 and α to compute the projected feed blockage:

$$P_0 = 2\frac{f}{D}D = 6 \text{ m} \quad \frac{0.415}{4c} = \frac{0.0577}{P}$$

$$D_{fb} = \frac{2P_0 \sin(\pi - \alpha)}{1 - \cos(\pi - \alpha)} = \frac{12 \sin \tan^{-1}(0.0577/P_0)}{1 + \cos \tan^{-1}(0.0577/P_0)}$$

The subreflector blockage is given by Eq. (8-67) also:

$$\psi_0 = 2 \tan^{-1} \frac{1}{4(0.3)}$$

$$D_s = \frac{2(1.5)P_0 \sin(\pi - \psi_0)}{1 - 1.5 \cos(\pi - \psi_0)} = 2.322P_0$$

We equate these blockages and solve the transcendental equation for P numerically:

$$P_0 = 0.385 \text{ m}$$

$$D_s = 0.894 \text{ m} \quad \text{subreflector diameter}$$

$$2c = 1.386 \text{ m} \quad \text{distance between subreflector foci}$$

We read the blockage loss from Table 4-40 using the Gaussian distribution, 0.14 dB. A Gregorian subreflector designed by parallel steps has a diameter about 6 cm larger and has about 0.02 dB more blockage loss.

Since the phase centers of most horns lie inside the bell along the axis, we move the feed horn toward the subreflector and increase the shadow blockage of the feed on the main reflector. We find the parameters of the reflector system to equalize feed shadowing to subreflector blockage by accounting for the phase-center distance D_{pc} and the diameter of the feed horn D_f by solving a quadratic equation. Given the main reflector diameter D , focal length f , and subreflector half subtended angle θ_0 , we solve the quadratic equation for roots X_1 [32]:

$$[8fD - \sigma \tan \theta_0(16f^2 - D^2)]X_1^2 - 16D_{pc} \tan \theta_0 fDX_1 - 16D_f f^2 D \tan \theta_0 = 0$$

The parameter σ equals -1 for a Cassegrain dual reflector and $+1$ for a Gregorian system. We use X_1 to solve for c , the focal length of the conic-section subreflector:

$$c = X_1 \frac{8fD - \sigma \tan \theta_0(16f^2 - D^2)}{32fD \tan \theta_0}$$

We compute e from the magnification factor from the effective f/D [Eq. (8-64)] or from the feed half-subtended angle θ_0 and the main half-subtended angle ψ_0 [Eq. (8-63)]. The rest of the parameters of the dual-reflector antenna follow from these parameters. The dual-reflector antenna geometry can be found from various other specified parameters [32].

8-13.2 Diffraction Loss [3, 6, 9, 33]

We cannot decrease the subreflector size to reduce the central blockage without penalty. We based the subreflector design on geometric optics (GO), which assumes large reflectors in terms of wavelengths. We size the subreflector to have all the spillover and none from the main reflector based on GO. The finite subreflector size produces diffractions that cause main-reflector spillover, cross-polarized subreflector reflections, phase error losses, and additional amplitude taper losses. We lump these excess losses into a diffraction loss term.

Rusch [3,33] finds these losses by using vector diffraction theory of PO where he calculates the currents on the subreflector. Similar results can be calculated by using GTD methods [6]. The results of GTD calculations for a circularly polarized feed are listed in Table 8-4. They are similar to the results given for a TE_{11} -mode circular horn feed [9]. The loss depends on the effective focal length and the diameter of the subreflector. Increasing the feed taper lowers the diffraction loss but it has a broad flat optimum at about a 12-dB edge taper. Equalizing the feed and subreflector blockage may not lead to the optimum (highest-gain) design. We must trade off diffraction loss and blockage loss.

Example Optimize the 10-m-diameter Cassegrain dual reflector for the sum of diffraction and blockage losses at 3.9 GHz.

TABLE 8-4 Diffraction Loss of a Cassegrain Antenna with a 10- and a 15-dB Feed Edge Amplitude Taper (dB)

Subreflector Diameter (λ)	Effective f/D					
	0.75	1.00	1.5	2.0	2.5	3.0
<i>For 10 dB</i>						
6	0.67	0.81	1.02	1.43	1.85	2.28
8	0.55	0.68	0.78	1.09	1.41	1.75
10	0.48	0.58	0.64	0.89	1.14	1.40
12	0.43	0.51	0.55	0.76	0.97	1.17
14	0.39	0.46	0.48	0.67	0.84	1.01
16	0.36	0.42	0.43	0.60	0.75	0.88
20	0.31	0.37	0.36	0.50	0.62	0.72
30	0.24	0.27	0.25	0.37	0.45	0.49
40	0.20	0.24	0.20	0.30	0.36	0.39
60	0.16	0.20	0.12	0.22	0.27	0.28
100	0.11	0.15	0.09	0.17	0.20	0.22
<i>For 15 dB</i>						
6	0.53	0.66	0.91	1.29	1.72	2.17
8	0.42	0.54	0.68	0.96	1.29	1.64
10	0.36	0.45	0.55	0.77	1.02	1.30
12	0.32	0.39	0.46	0.65	0.85	1.07
16	0.26	0.31	0.36	0.49	0.63	0.78
20	0.22	0.27	0.29	0.40	0.51	0.62
50	0.12	0.15	0.13	0.19	0.22	0.24
100	0.07	0.10	0.11	0.12	0.14	0.14

TABLE 8-5 Subreflector Diameter Trade-off

Diameter (λ)	Blockage (dB)	Diffraction Loss (dB)	Sum (dB)
11.6	0.14	0.57	0.71
14.0	0.20	0.48	0.68
16.0	0.26	0.43	0.69
18.0	0.33	0.40	0.73

The subreflector diameter is 0.894 m, or 11.62λ . We can increase the subreflector diameter without affecting the results of the preceding example, and the feed blockage will be less than the subreflector blockage. We generate Table 8-5 from Tables 4-40 and 8-4. The optimum occurs at about 15λ diameter, or 1.154 m. The table shows a broad optimum, with variations of $\pm\lambda$ having no practical effect. We move the feed back to illumine the larger subreflector:

$$2c = 3.6P = \frac{3.6D_s}{2.322} = 1.789 \text{ m}$$

Kildal [34] has derived a simple formula for the optimum subreflector size to minimize the combination of blockage and diffraction losses:

$$\frac{d}{D} = \left[\frac{\cos^4(\theta_0/2)}{(4\pi)^2 \sin \psi_0} E \frac{\lambda}{D} \right]^{1/5}$$

where d is the subreflector diameter, D the main-reflector diameter, and E the power illumination at the edge of the subreflector (0.1 for 10 dB). The approximate product of the efficiencies (blockage and diffraction) at the optimum d/D is

$$\eta \approx \left\{ 1 - C_b \left[1 + 4\sqrt{1 - \frac{d}{D}} \right] \left(\frac{d}{D} \right)^2 \right\}^2$$

where $C_b = -\ln \sqrt{E}/(1 - \sqrt{E})$. This analysis gives a good first estimate of the proper subreflector size and associated loss. Beyond this rule, extending the subreflector diameter by 1λ to 2λ beyond the GO design reduces the diffraction loss of a Cassegrain significantly even though the blockage loss increases. The reduction in diffraction is much greater than the increased blockage loss. This approach does not work with a Gregorian reflector, because it already has a lower diffraction loss, due to the convex subreflector.

8-13.3 Cassegrain Tolerances [9, 35]

To calculate the feed movement effects, reduce them by the magnification factor M and use the f/D value of the main reflector. The result is the reduction of the tight location tolerances normally required of the deep (small f/D) main reflector. For feed scanning we must multiply the offset required for the main reflector by the magnification factor to compute the necessary lateral offset. Translation of the hyperboloid is nearly equivalent

TABLE 8-6 Scale Factor for RMS Surface Deviations of a Dual Reflector

Eccentricity, e	Main Reflector, f/D					
	0.25	0.30	0.35	0.40	0.45	0.50
0.5	1.259	1.183	1.136	1.105	1.083	1.068
0.6	1.203	1.143	1.107	1.082	1.066	1.053
0.7	1.148	1.105	1.078	1.060	1.048	1.039
0.8	1.096	1.068	1.051	1.039	1.031	1.026
0.9	1.046	1.033	1.024	1.019	1.015	1.012
1.0	1.000	1.000	1.000	1.000	1.000	1.000
1.2	0.919	0.941	0.956	0.965	0.972	0.977
1.5	0.821	0.868	0.900	0.921	0.937	0.948
2.0	0.707	0.780	0.830	0.865	0.891	0.910
2.5	0.632	0.718	0.780	0.824	0.857	0.882
3.0	0.580	0.674	0.743	0.794	0.832	0.860

Source: [36].

TABLE 8-7 Scale Factor for Random Normal Surface Deviations Δn of a Dual Reflector

Eccentricity, e	Main Reflector f/D					
	0.25	0.30	0.35	0.40	0.45	0.50
0.5	0.872	0.898	0.918	0.933	0.944	0.953
0.6	0.834	0.868	0.894	0.914	0.929	0.940
0.7	0.796	0.839	0.871	0.895	0.913	0.928
0.8	0.759	0.811	0.849	0.877	0.899	0.915
0.9	0.725	0.784	0.828	0.860	0.885	0.904
1.0	0.693	0.759	0.808	0.844	0.872	0.893
1.2	0.637	0.715	0.772	0.815	0.847	0.872
1.5	0.569	0.660	0.727	0.778	0.816	0.846
2.0	0.490	0.592	0.671	0.730	0.777	0.812
3.0	0.402	0.512	0.600	0.670	0.725	0.768

to a movement of the virtual feed but it is reduced by the factor $(M - 1)/M$. Rotating the subreflector laterally offsets the virtual feed by the factor $2c\beta/(M + 1)$, where $2c$ is the distance from the feed to the virtual feed and β is the rotation (radians). Since all factors are small, we can add them.

The surface tolerance of the subreflector adds another phase error loss term in the same form as the main reflector. The tolerance loss factor is less for a hyperbola than for a parabola because the angles of incidence are higher [36]. The ellipsoid of the Gregorian reflector has higher losses. We express the loss at each reflector as

$$\text{PEL} = e^{-A(4\pi\Delta\varepsilon/\lambda)^2} \quad (8-68)$$

where $\Delta\varepsilon$ is the RMS deviation to the perfect reflector surface and A is a constant depending on the eccentricity of the reflector and the main reflector f/D . This factor

is listed in Table 8-6. The main reflector has $e = 1$ (parabola). An equation matching Eq. (8-24) is

$$\text{PEL(dB)} = -685.8A \left(\frac{\Delta\epsilon}{\lambda} \right)^2 \quad (8-69)$$

The factor $\Delta\epsilon$ is the change in path length along a ray due to the surface deviation [Eq. (8-23)]. It is easier to specify the surface deviation in the normal direction for a subreflector. Table 8-7 gives the scale factor in terms of the normal directed surface deviation.

8-14 FEED AND SUBREFLECTOR SUPPORT STRUT RADIATION

Feed or subreflector support struts block the aperture of a centrally fed reflector and reduce gain. Because the passing waves induce currents on the struts that radiate, the effect of struts can be larger than their area. Thin struts, like thin dipoles, have a significant effective area as an antenna. The radiation from struts generates sidelobes and cross-polarization that degrade the reflector pattern. We approach strut analysis either by increasing their effective area due to the induced currents or by using physical optics to add the induced currents to the pattern, or use a ray optics method, such as GTD, to find the total pattern.

Strut losses and stray radiation should be small in a properly designed reflector, but mechanical considerations may lead to less than ideal electrical configurations. If possible, attach the struts to the outer rim of the reflector. When mounted part-way out of the radius, the struts can support the feed or subreflector with thinner elements, but they block the feed (or subreflector) radiation and cast a shadow on the main reflector. Of course, when struts pass through the main reflector, they can be mounted to a smaller support frame located behind the reflector and the final design will be a compromise. Symmetrically oriented struts reduce boresight cross-polarization. For linear polarization, use four struts aligned parallel and perpendicular to the polarization vector to reduce cross-polarization at all angles. Thorough analysis considers the currents induced on the struts due to the feed radiation. These strut currents radiate and illuminate the main or subreflector along with the feed because the primary strut effect is blocking the nearly plane wave radiated by the main reflector.

Kay [37] introduced the induced field ratio (IFR) to analyze space metal frame radomes. The IFR hypothesis assumes that the currents induced on the strut are the same as those on an infinite strut illuminated by a plane wave. This reduces the problem to two dimensions. Currents induced on a thin strut increase the effective blockage area by the IFR factor. We sum these blockage areas projected on the aperture plane without regard to phase. IFR is the forward-scattered field divided by the radiation from a plane wave incident on the same area (i.e., an aperture). This reduces the complicated radiation from the strut to a simple blocked area. IFR depends on the incident polarization, and since it is a two-dimensional problem, we have only TM (E -field parallel to strut axis) or TE (H -field parallel to axis) waves.

The TM wave induces currents directed along the axis that we compute either by using a canonical problem with a closed-form solution or by using the method of moments with an incident plane. Given the surface current density $J_s(\phi)'$, a function

of the angle from the incident plane wave ϕ' on a strut cross section $\rho(\phi')$, the TM wave IFE_E can be found from an integral around the strut perimeter:

$$\text{IFR}_E = -\frac{\eta}{2wE_0} \int_{S_1} J_s(\phi') e^{-jk\rho(\phi')} \rho(\phi') d\phi' \quad (8-70)$$

The strut has a projected width w normal to the incident plane wave with electric field E_0 and η is the impedance of free space.

The TE wave induces currents that flow around the perimeter. We describe the current by the z -directed magnetic field on the strut. Given a unit vector \mathbf{a}_f in the forward direction and the surface normal $\mathbf{n}(\phi')$, IFR_H is found from an integral around the strut:

$$\text{IFR}_H = \frac{1}{2wH_0} \int_{S_1} [\mathbf{a}_f \cdot \mathbf{n}(\phi')] H_z(\phi') e^{-jk\rho(\phi')} \rho(\phi') d\phi' \quad (8-71)$$

We calculate effective strut blockage area by multiplying the projected area of the strut in the aperture by IFR and use Eq. (4-111) for the loss. For a linearly polarized wave at an angle γ_i to the projected strut, we use an elliptical addition of the area:

$$\text{area} = \sum_{i=1}^N w_i (\text{IFR}_{Ei} \cos^2 \gamma_i + \text{IFR}_{Hi} \sin^2 \gamma_i) \quad (8-72)$$

We use the mean $\text{IFR}_M = (\text{IFR}_E + \text{IFR}_H)/2$ for circular polarization. The difference $\text{IFR}_D = (\text{IFR}_E - \text{IFR}_H)/2$ is a useful quantity for estimating the sidelobes and cross-polarization.

Given a reflector of radius r_0 and symmetrically placed N struts which reduces cross-polarization, we define the strut factor A_{co} as IFR times the ratio of the projected area of one strut to the reflector area:

$$A_{co} = |\text{IFR}_i| \frac{N_p w' r_0}{\pi r_0^2} \quad (8-73)$$

with $w' = w \sin \theta_0$, the width projected along the plane wave,

$$N_p = \begin{cases} 1 & \text{for } N \text{ odd} \\ 2 & \text{for } N \text{ even} \end{cases}$$

and

$$|\text{IFR}_i| = \begin{cases} |\text{IFR}_M| & \text{for circular polarization} \\ |\text{IFR}_M - \text{IFR}_D \cos 2\gamma_i| & \text{for linear polarization} \end{cases}$$

Blockage co-polarization sidelobes due to the struts radiate a broad pattern that reaches an asymptotic level [38]:

$$\text{sidelobe(dB)} = \begin{cases} 20 \log(A_{co}) & \text{for uniform aperture} \\ 20 \log(A_{co}) - 2 & \text{for } -20\text{-dB taper aperture} \end{cases} \quad (8-74)$$

The maximum cross-polarization within the 3-dB beamwidth can be found from the difference IFR_D . Define the cross-polarization strut factor:

$$A_{\text{xp}} = |\text{IFR}_D| \frac{N_p w' r_0}{\pi r_0^2}$$

For three struts the cross-polarization(dB) = $20 \log(A_{\text{xp}}) + 2.5$, and for four struts cross-polarization(dB) = $20 \log(A_{\text{xp}}) - 8.5$ for a uniform distribution and $20 \log(A_{\text{xp}}) - 7$ with a 20-dB aperture taper [38].

Closed-form equations for IFR exist for circular struts [39] that depend on the angle between the strut axis and the incident plane wave θ_0 , the strut radius a , and the propagation constant k :

$$\begin{aligned} \text{IFR}_E &= -\frac{1}{ka \sin \theta_0} \sum_{n=0}^{\infty} \varepsilon_n \frac{J_n(ka \sin \theta_0)}{H_n^{(2)}(ka \sin \theta_0)} \\ \text{IFR}_H &= -\frac{1}{ka \sin \theta_0} \sum_{n=0}^{\infty} \varepsilon_n \frac{J_n'(ka \sin \theta_0)}{H_n^{(2)'}(ka \sin \theta_0)} \\ \varepsilon_n &= \begin{cases} 1 & \text{for } n = 0 \\ 2 & \text{for } n > 0 \end{cases} \end{aligned} \quad (8-75)$$

where J_n is the Bessel function and $H_n^{(2)}$ is the outward-traveling Hankel function, with J_n' the derivative of J_n , and so on. Table 8-8 lists these factors for both polarizations versus strut radius.

Using only physical optics we can determine accurately the blockage effects of struts that are at least 3λ in diameter. PO excites currents only on the visible half of the struts. For smaller-diameter struts, currents creep to the far side and alter the results. No matter how thin the struts, currents will be excited on them and affect the pattern. The physical optics analysis of a dual reflector includes currents excited on the struts a number of times. Assume that the antenna is transmitting. The feed illuminates the subreflector and the struts. The current excited on the struts also radiates a field that illuminates the subreflector. If the strut blocks the path between the feed and the subreflector, PO analysis uses strut current to calculate its blockage. At this point we use the currents

TABLE 8-8 IFR_E and IFR_H for a Circular Strut

$a \sin \theta_0$	$\text{Re}(\text{IFR}_E)$	$\text{Im}(\text{IFR}_E)$	$\text{Re}(\text{IFR}_H)$	$\text{Im}(\text{IFR}_H)$
0.005	-5.148	14.088	-0.0001	-0.0198
0.010	-3.645	6.786	-0.0005	-0.050
0.020	-2.712	3.964	-0.004	-0.103
0.050	-1.982	2.003	-0.054	-0.272
0.10	-1.641	1.225	-0.292	-0.448
0.20	-1.414	0.758	-0.552	-0.374
0.50	-1.215	0.381	-0.781	-0.258
1.00	-1.145	0.255	-0.858	-0.188
2.00	-1.092	0.160	-0.914	-0.126

on the subreflector to compute additional currents excited on the struts. These add to the first set of strut currents. Radiation from the subreflector, all currents on the struts, and stray feed illumination add to illuminate the main reflector. The radiation from the main reflector current excites additional current on the subreflector and a third set of currents on the struts. We apply the far-field Green's function on the sum of all currents to calculate the pattern.

PO currents are modified on thin struts to account for creeping-wave currents. We multiply the PO strut currents by the induced current ratio (ICR) to obtain equivalent currents suitable for predictions. The factor ICR includes a strut current distribution and a complex value:

$$\mathbf{J}_s = 2\mathbf{n} \times \mathbf{H}_{\text{inc}} \cdot \text{ICR}(a, \theta_0, \phi') \quad (8-76)$$

ICR depends on the strut radius a , the incidence angle θ_0 with respect to the strut axis, and the angle around the strut ϕ' from the direction of the plane wave and the incident wave polarization. We find the incident magnetic field \mathbf{H}_{inc} at the point where the plane wave touches the strut and use the current excited at this point to calculate the current in a ring around the strut. Remember that the primary effect of the strut is to block the radiation from the main reflector that approximates a plane wave in the near field where the struts are located.

We solve for ICR by considering two-dimensional scattering of the strut cross section by a plane wave. By applying moment methods to a two-dimensional scattering problem, we can solve for the current distribution on any strut cross section, but here we consider only circular struts that have a closed-form solution [40, pp. 209–219]. To simplify the problem, consider a strut lying along the z -axis. For actual analysis you will need to rotate the strut into place and rotate the incident wave into the strut coordinate system to use ICR to calculate the current distribution. In two-dimensional space the incident wave is either TM or TE with respect to the z -axis. The TM wave has its electric field in the plane containing the strut axis. A TE wave has its magnetic field in this plane. The TM case produces the following equation from the scattering of a plane wave:

$$\text{ICR}_E \hat{\mathbf{z}} = \text{ICR}_{\text{TM}}(a, \theta_0, \phi') \hat{\mathbf{z}} = \frac{\hat{\mathbf{z}} e^{-jka \cos \phi'}}{\pi ka \sin \theta_0} \sum_{m=0}^{\infty} \frac{j^m \varepsilon_m \cos m\phi'}{H_m^{(2)}(ka \sin \theta_0)} \quad (8-77)$$

The phase factor $e^{-jka \cos \phi'}$ shifts the reference plane from the strut center to the attachment point. Equation (8-77) expands the current in a $\cos m\phi'$ Fourier series around the strut. ICR_E has a complex value because $H_m^{(2)}$ has a complex value. As the strut radius a increases, ICR approaches 1 at the location $\phi' = 0$. For practical purposes ICR is 1 for $a/\lambda > 1.5$.

Equation (8-77) gives the current distribution on the circular strut relative to the current excited at the initial contact point of the incident plane wave. Table 8-9 lists ICR_E evaluated when $\phi' = 0$. The constant term grows rapidly as $a \rightarrow 0$, with its imaginary part growing faster than the real part because it approximates the vector potential of a filamentary current element with its $-j$ factor between the current and the field [Eq. (2-1)]. Small struts have nearly constant current around their periphery. Equation (8-77) requires more and more terms as the strut diameter increases, and finally, a simple PO solution produces the same results. Table 8-9 lists the ICR factors versus the strut radius.

TABLE 8-9 ICR_E and ICR_H PO Current Multipliers When $\phi' = 0$ for a Circular Strut

$a \sin \theta_0$	Re(ICR _E)	Im(ICR _E)	Re(ICR _H)	Im(ICR _H)
0.002	3.660	-7.932	0.500	0.003
0.004	2.735	-4.530	0.500	0.013
0.01	2.018	-2.228	0.499	0.033
0.02	1.687	-1.353	0.500	0.071
0.05	1.376	-0.751	0.546	0.195
0.10	1.200	-0.479	0.748	0.275
0.50	1.030	-0.140	0.948	0.109
1.00	1.010	-0.076	0.982	0.068
1.50	1.005	-0.052	0.991	0.049

A TE incident wave produces similar results for scattering from a circular cylinder but has co- and cross-polarization terms:

$$\text{ICR}_H = \text{ICR}_{\text{TE}}(a, \theta_0, \phi') \hat{\phi} = \frac{j \hat{\phi} e^{-jka \cos \phi'}}{\pi ka \sin \theta_0} \sum_{m=0}^{\infty} \frac{j^m \varepsilon_m \cos m\phi'}{H_m^{(2)'}(ka \sin \theta_0)} \quad (8-78)$$

Equation (8-78) has the same form as Eq. (8-77) and is expanded in the even function $\cos m\phi'$ as Eq. (8-77) with coefficients using the derivative of the Hankel function.

When the incident wave approaches the strut at an angle θ_0 other than 90° , the strut scatters cross-polarization for a TE incident wave:

$$\text{JCR}_H = \text{JCR}_{\text{TE}} \hat{\mathbf{z}} = \frac{j \cos \theta_0 \hat{\mathbf{z}} e^{-jka \cos \phi'}}{(ka \sin \theta_0)^2} \sum_{m=-\infty}^{\infty} \frac{m j^m e^{jm\phi'}}{H_m^{(2)'}(ka \sin \theta_0)} \quad (8-79)$$

JFR_H is an odd function around the perimeter of the strut with a zeroth term of zero. We can expand Eq. (8-79) in terms of $\sin m\phi'$:

$$\text{JCR}_H = \frac{-2j \cos \theta_0 \hat{\mathbf{z}} e^{-jka \cos \phi'}}{(ka \sin \theta_0)^2} (I_1' \sin \phi' + j2I_2' \sin 2\phi' - 3I_3' \sin 3\phi' - \dots)$$

$$I_m' = \frac{1}{H_m^{(2)'}(ka \sin \theta_0)} \quad (8-80)$$

Consider a plane wave incident on a straight strut at an angle θ_0 to its axis. As the wave sweeps across the strut it excites current whose phase velocity is $c/\cos \theta_0$ with respect to the strut axis. This is the same situation as a waveguide with two waves traveling back and forth between the sidewalls that produces a central phase velocity greater than c (Section 5-24). A thin strut with its constant current distribution around the circumference radiates a cone-shaped pattern peaked at an angle determined by the current phase velocity. The current is a fast or leaky wave radiator that radiates in a cone at an angle θ_0 from the axis, while the length of the strut in wavelengths determines the narrowness of the radiation beamwidth. As the diameter of the strut increases, the peripheral current distribution alters the radiation level around the cone, but the peak radiation occurs along the cone determined by the incident angle.

We use incident plane waves to derive strut blockage and scattering and to modify the formulation for spherical wave incidence. First divide the struts into coin sections. For a wave incident from a given point, we trace a ray from the point to the strut axis through a given coin section. We determine the incident magnetic field and calculate the surface current density at the point of intersection of this ray and the strut. The intersection point is $\phi' = 0$. We apply ICR_E , ICR_H , and JCR_H to calculate the currents around the coin cross section. This near-field case does not radiate a strut cone pattern because it is not a plane wave incident on the strut. As the strut diameter grows, this method leads directly to a PO formulation for strut scattering.

8-15 GAIN/NOISE TEMPERATURE OF A DUAL REFLECTOR

Collins [41] has developed a procedure for calculating the noise temperature of Cassegrain antennas pointed near the horizon. First, the diffraction pattern of the feed and subreflector combination is calculated. Some of the diffraction is added to the main-reflector spillover. At low elevation angles the antenna points about one-half of the spillover on the ground. It is a major noise temperature contribution, $\frac{1}{2}(1 - \text{SPL})T_G$, where T_G is the ground temperature and SPL is the spillover efficiency (ratio). The scattered portion of the blockage produces wide-angle sidelobes, half of which see the ground. The gain is reduced by the spillover loss, and a uniform distribution for the blockage is assumed ($\text{ATL} = 1$):

$$\frac{1}{2} \frac{S_b}{S_a} (\text{SPL}) T_G$$

where S_b is the blocked area and S_a is the total potential aperture. The main beam points toward the sky and collects noise, $\text{SPL} \eta_b \eta_m T_s$, where η_b is the blockage efficiency, η_m the ratio of the power in the main beam and the first few sidelobes ($\eta_m \approx 0.99$), and T_s the sky temperature. We include a group of minor contributors:

$$\frac{1}{2} (1 - \text{SPL}) T_s \quad \frac{1}{2} \frac{S_b}{S_a} (\text{SPL}) T_s \quad \frac{1}{2} \text{SPL} \eta_b (1 - \eta_m) (T_G + T_s)$$

Equation (1-56) can be used when the temperature distribution is known, but the procedure of Collins gives good, although slightly conservative results. Refer to Section 1-15 to calculate the gain noise temperature of the receiving system.

8-16 DISPLACED-AXIS DUAL REFLECTOR

A displaced-axis dual reflector uses a paraboloidal main reflector with a ring focus that transforms the vertex into a ring. GO rays reflected from the main paraboloid miss the subreflector and reduce the blockage loss to a nonexcitation area instead of scattered blockage. This reflector achieves high aperture efficiency by using a subreflector that directs the higher feed radiation at the boresight to the outer rim of the parabola, where the differential area is the largest.

For the moment, consider Figure 8-14 of the Gregorian dual reflector in two dimensions. The parabola and ellipse retain their reflecting properties because we can extend them out of the page into cylindrical reflectors and use a linear array as a feed. Mentally, remove the lower half of the parabola and the upper half of the ellipse. Rays

from the left ellipse focus (feed) reflect from the remaining half of the lower ellipse to the upper half of the parabola, which transforms them into plane waves. If we fix the right ellipse focus at the focus of the parabola, we can rotate the ellipse axis about the right focus without changing the ray tracing from a feed at the left focus. We use a slightly different portion of the ellipse determined by the rays traced to the edges of the remaining half parabola.

Place a horizontal axis at the lower edge of the ellipse and rotate the ellipse axis until the feed focus is on this axis. Rotate the two-dimensional figure about this horizontal axis to form a three-dimensional reflector, and it becomes a displaced-axis dual reflector. Both the focus and vertex of the main reflector have become rings. The subreflector has a matching ring focus at the same diameter as that of the main vertex and a point focus at the feed (Figure 8-16). Now rays from the upper portion of the subreflector reflect to the upper portion of the parabola. Rays from the center of the subreflector terminate on the outer edge of the main reflector, while outer subreflector edge rays reflect to the ring vertex of the main reflector [42].

The reflector geometry has been found in closed form [43]. Given the main reflector diameter D , focal length f , diameter of the subreflector D_s , and feed half-subtended angle θ_0 , the distance along the reflector axis from the vertex to the feed L_m is

$$L_m = \frac{fD}{D - D_s} - \frac{D_s \cos \theta_0 + 1}{4 \sin \theta_0} \quad (8-81)$$

We tilt the axis of the ellipse ϕ to collapse the ring focus to a point at the feed:

$$\tan \phi = \frac{2}{(\cos \theta_0 + 1)/\sin \theta_0 - 4f/(D - D_s)} \quad (8-82)$$

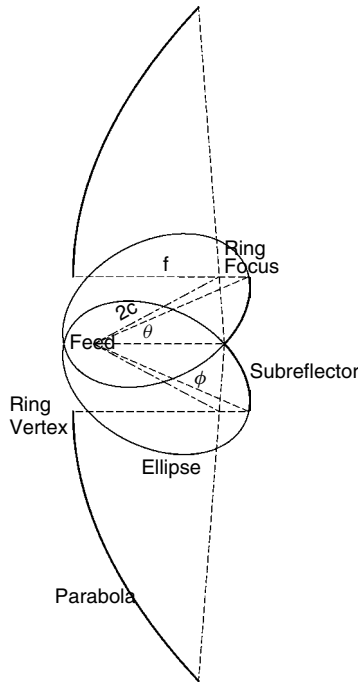


FIGURE 8-16 Displaced-axis reflector antenna.

The parameters of the ellipse are given by the equations

$$c = \frac{D_s}{4 \sin \phi} \quad \text{and} \quad a = \frac{D_s}{8} \left(\frac{\cos \theta_0 + 1}{\sin \theta_0} + \frac{4f}{D - D_s} \right) \quad (8-83)$$

The half-subtended angle of the main reflector ψ_0 is found from the normal parabola with the subreflector removed and the ring focus collapsed to a point [Eq. (8-2)]:

$$\psi_0 = 2 \tan^{-1} \frac{D - D_s}{4f}$$

We compute the distance between the feed and the subreflector along the axis L_s from the geometry [45]:

$$L_s = 2c \cos \phi + \frac{D_s}{2 \tan \psi_0}$$

We determine aperture power distribution $A(r')$ by tracing rays from the feed to the aperture radius r' of the main reflector and by equating power in differential areas:

$$P(\theta) \sin \theta d\theta = A(r') dr' \quad (8-84)$$

Figure 8-17 gives the aperture distribution for a displaced-axis reflector designed for a main reflector $f/D = 0.27$ and an effective $f_{\text{eff}}/D = 1.2$ from the feed ($\theta_0 = 23.54^\circ$) for various feed edge tapers. The plot shows that increasing the feed edge taper increases the aperture power at larger radii but reduces the center amplitude. The center 20% of the diameter of the aperture is not excited, but this corresponds to only 4% lost area, or -0.18 dB. When calculating the amplitude taper loss [Eq. (4-8)], we

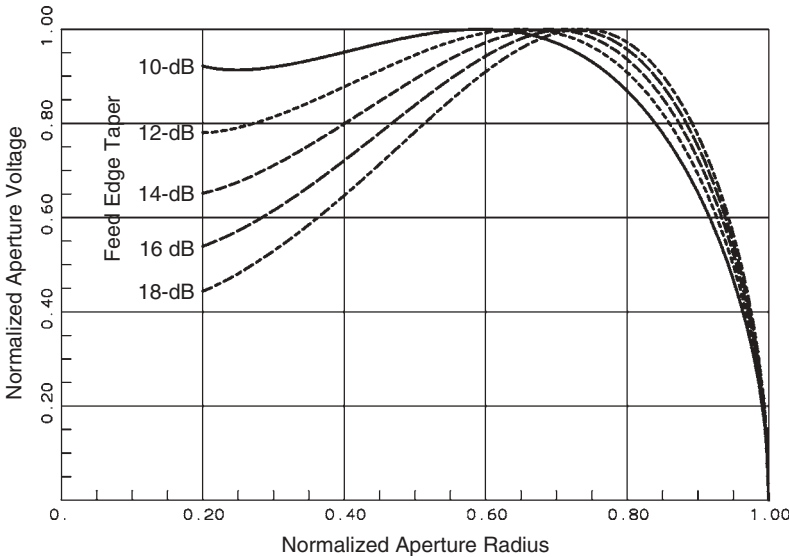


FIGURE 8-17 Aperture distribution in a displaced-axis reflector given feed edge taper for a particular antenna. (From [43], Fig. 3, © 1997 IEEE.)

TABLE 8-10 Illumination Losses of a Displaced-Axis Dual Reflector, $f/D = 0.27$, $f_{\text{eff}}/D = 1.2$ for $D_s = 0.2D$ and $0.1D$ Versus a Feed Edge Taper

Edge Taper (dB)	D_s/D (%)							
	20				10			
	SPL (dB)	ATL (dB)	Total (dB)	Sidelobe	SPL (dB)	ATL (dB)	Total (dB)	Sidelobe
10	0.434	0.476	0.910	15.2	0.434	0.411	0.845	18.3
11	0.341	0.455	0.796	14.9	0.341	0.377	0.718	17.8
12	0.268	0.442	0.710	14.5	0.268	0.350	0.619	17.3
13	0.212	0.434	0.646	14.2	0.212	0.330	0.542	16.8
14	0.167	0.432	0.600	14.0	0.167	0.316	0.483	16.4
15	0.132	0.436	0.568	13.7	0.132	0.308	0.440	16.0
16	0.105	0.444	0.548	13.5	0.105	0.304	0.409	15.6
17	0.083	0.456	0.539	13.3	0.083	0.306	0.388	15.3
18	0.066	0.472	0.537	13.1	0.066	0.311	0.377	14.9
19	0.052	0.491	0.543	12.9	0.052	0.320	0.372	14.6
20	0.041	0.513	0.555	12.7	0.041	0.333	0.374	14.3

use the full radius $a = D/2$, which accounts for the lost aperture center area. Table 8-10 lists the illumination losses of this reflector. The antenna has 88.2% aperture efficiency, including blockage loss for $D_s/D = 0.2$ and 91.8% for $D_s/D = 0.1$. These numbers do not include diffraction loss due to the subreflector and main reflector size in wavelengths or strut blockage. Similar to a Cassegrain reflector, increasing the subreflector diameter beyond the GO design by 1 to 2λ decreases the diffraction loss.

Figure 8-17 shows the complete taper of the aperture to zero voltage at the edge. We can increase the aperture efficiency slightly by designing the antenna with an effective main reflector diameter slightly larger than the real diameter and produce a finite aperture edge taper at the cost of increased spillover past the main reflector. Table 8-11 lists the illumination losses for designs the same as Table 8-10 except that the effective main reflector is 2% greater.

Four versions of displaced-axis reflectors have been derived from Gregorian and Cassegrain antennas [44]. One other case, the double-offset Cassegrain, crosses the feed illumination so that boresight feed amplitude reflects to the outer rim of the main reflector. This antenna, similar to the case covered above, has a high aperture efficiency, whereas the other two cases have modest aperture efficiencies. Equations to specify all four antennas are available [45]. The normal displaced-axis dual reflector has less sensitivity to feed axial defocusing than does a normal Cassegrain or Gregorian antenna, but it is more sensitive to lateral offset of the feed [46].

8-17 OFFSET-FED DUAL REFLECTOR

When we offset-feed a dual reflector, we can eliminate subreflector central blockage of the Cassegrain or Gregorian reflectors. This design adds parameters to give more convenient packaging that fits in the available space, such as on a spacecraft. More important, by rotating the subreflector axis relative to the main reflector axis, we can

TABLE 8-11 Illumination Losses of a Displaced-Axis Dual Reflector, $f/D = 0.27$, $f_{\text{eff}}/D = 1.2$ for $D_s = 0.2D$, and $0.1D$ Versus a Feed Edge Taper (Effective Main Diameter = 102% Actual)

Edge Taper (dB)	D_s/D (%)							
	20				10			
	SPL (dB)	ATL (dB)	Total (dB)	Aperture Taper (dB)	SPL (dB)	ATL (dB)	Total (dB)	Aperture Taper (dB)
10	0.455	0.371	0.816	10.6	0.443	0.304	0.746	13.5
11	0.352	0.352	0.705	10.4	0.350	0.271	0.621	12.5
12	0.280	0.340	0.621	10.1	0.278	0.246	0.524	11.5
13	0.225	0.335	0.559	9.9	0.222	0.227	0.449	10.6
14	0.181	0.334	0.515	9.6	0.178	0.215	0.393	10.4
15	0.147	0.339	0.486	9.5	0.144	0.208	0.352	10.2
16	0.120	0.349	0.469	9.3	0.117	0.206	0.323	10.0
17	0.099	0.363	0.462	9.1	0.096	0.209	0.305	9.8
18	0.083	0.380	0.463	9.0	0.079	0.216	0.295	9.7
19	0.070	0.401	0.471	8.8	0.066	0.227	0.293	9.5
20	0.060	0.425	0.485	8.7	0.056	0.241	0.297	9.4

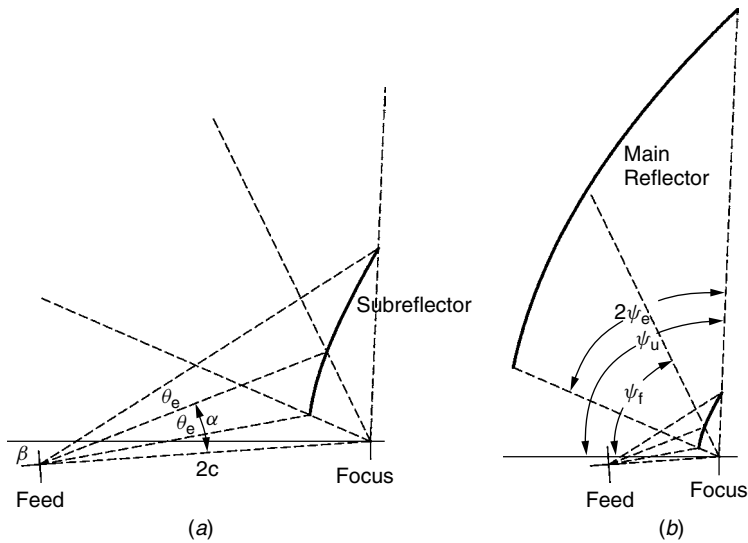


FIGURE 8-18 Dual offset-fed Cassegrain reflector, including Mizuguchi feed axis tilt: (a) feed and subreflector geometry; (b) dual reflector.

greatly reduce cross-polarization or beam squint of dual circularly polarized feeds in the offset reflector.

Figure 8-18 illustrates the geometry of an offset-fed Cassegrain reflector, and Figure 8-19 shows the offset-fed Gregorian geometry. Refer to Figure 8-7 for the parameters of the offset main reflector. We point the feed at the subreflector center to reduce spillover and to equalize the amplitude distribution in the aperture of the

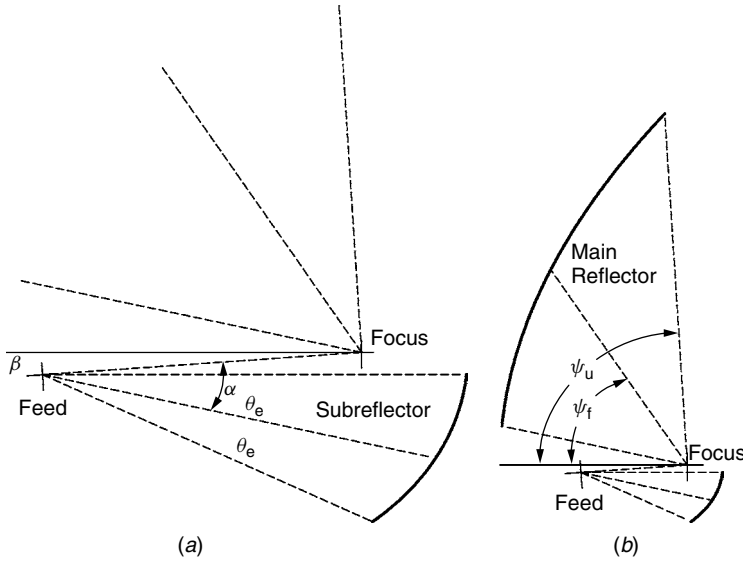


FIGURE 8-19 Dual offset-fed Gregorian reflector, including Mizugutch feed axis tilt: (a) feed and subreflector geometry; (b) dual reflector.

main reflector. Similar to a displaced-axis dual reflector, we tilt the axis between the focuses of the subreflector relative to the main reflector axis β (α in Ticra [48, App. B]). The small amount of tilt to the subreflector axis converts the equivalent parabola of the dual reflector to an axisymmetric geometry [47].

It takes five parameters to specify the antenna if the Mizugutch angle requirement is applied to the feed tilt angle α (ψ_0 Ticra) relative to the subreflector axis determined from the magnification M given the subreflector eccentricity e [Eq. (8-64)]:

$$M \tan \frac{\beta}{2} = \tan \frac{\alpha}{2} \quad \text{or} \quad \left(M \tan \frac{\alpha}{2} = \tan \frac{\psi_0}{2} \right)^{\dagger} \quad \text{for } M = \frac{e+1}{e-1} \quad (8-85)$$

The equation for M in Eq. (8-85) is used for both Cassegrain and Gregorian reflectors. We start the design with the diameter of the main reflector D because it determines the gain and beamwidth. Ticra [48, App. B] uses main reflector focal length f , the half distance between focuses of subreflector c , subreflector eccentricity e , and axis tilt β . Granet [49,50] supplies equations to calculate the reflector dimensions for 17 different sets of five input parameters. These sets of equations allow the direct application of various mechanical constraints to the design or electrical constraints, such as subreflector size to limit diffraction loss. All of Granet's sets apply the Mizugutch relationship, because this small change should be applied to all designs.

By tracing rays through the reflectors, the center offset H is found:

$$H = -2f \frac{\tan(\beta/2) - M \tan(\alpha/2)}{1 + M \tan(\beta/2) \tan(\alpha/2)} \quad (8-86)$$

Given H , D , and f , we compute main reflector parameters from Eqs. (8-35) to (8-47). We compute the half subtended angle of feed θ_e by tracing the ray to the upper rim of

the main reflector with feed angles ψ_U and α :

$$\psi_U = -2 \tan^{-1} \frac{2H + D}{4f} \quad \text{and} \quad \theta_e = \left| 2 \tan^{-1} \left(\frac{1}{M} \tan \frac{\psi_U - \beta}{2} \right) - \alpha \right| \quad (8-87)$$

The feed subtended angle of the subreflector is $2\theta_e$. We calculate the rim ellipse of the subreflector determined by the cone axis with angle α and cone angle θ_e using Eq. (8-59) and (8-60).

8-18 HORN REFLECTOR AND DRAGONIAN DUAL REFLECTOR

The horn reflector shown in Figure 8-20 consists of a pyramidal or conical input section excited with a rectangular or circular waveguide mode, respectively, that feeds an offset paraboloidal reflector. The beam exits horizontally. The horn reflector geometry is an offset reflector with offset angle $\psi_0 = 90^\circ$ and center offset $H = 2f$ the same as the periscope configuration. Figure 8-21 gives the pattern of a 3-m-diameter reflector operating at 6 GHz (diameter $= 60\lambda$) with $f = 3.215$ m ($\psi_e = 15^\circ$). The antenna radiates cross-polarization -23 dB relative to the beam peak in the horizontal plane. It cannot be used for two channels with different polarizations, because similar to all offset-fed reflectors, circularly polarized beams squint right and left in this horizontal plane. The antenna radiates a significant sidelobe 90° from the boresight in the horizontal plane that can be controlled using serrated-edge blinders [51].

A Dragonian dual reflector uses a hyperbola subreflector that curves toward the main reflector in a Cassegrain system. This produces a dual reflector with magnification

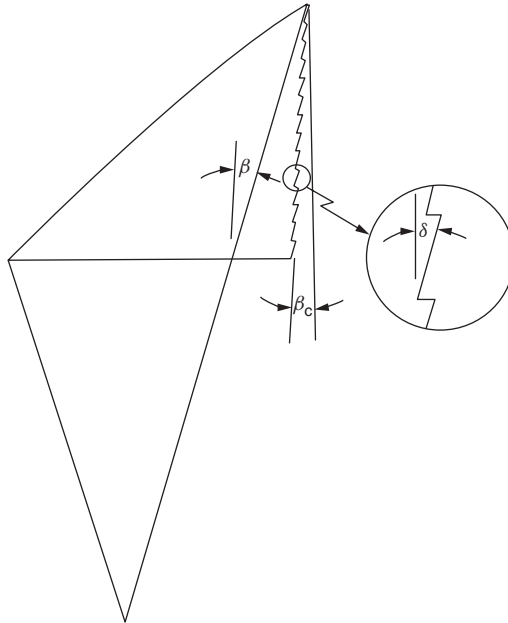


FIGURE 8-20 Horn reflector with serrated side blinders. (From [51], Fig. 3, © 1973 IEEE.)

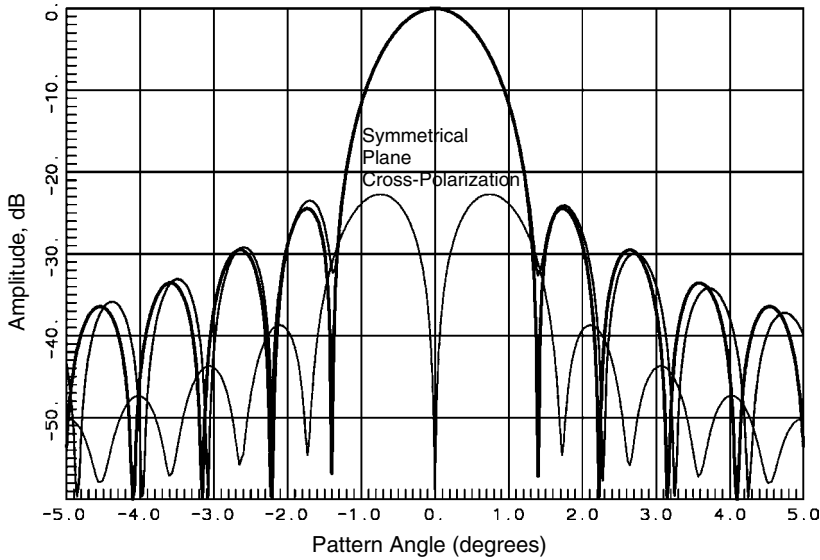


FIGURE 8-21 Pattern of a 3-m horn reflector at 6 GHz.

$M < 1$ and we need a feed antenna with a wider beamwidth than would be required for efficient feed of the main reflector. We use long focal lengths for the main reflector, which flattens its curve, so that the feed beamwidth can remain small. Jones and Kelleher [52] applied this Cassegrain arrangement to a horn reflector and located the feed horn in the middle of the paraboloidal main reflector. Dragone [53] derived the generalized Mizugutch criterion for multiple reflectors and showed that it could be applied to this Cassegrain system to eliminate cross-polarization. Figure 8-22 shows a Dragonian dual reflector fed by a corrugated horn feed located beyond the rim of the paraboloidal reflector to replace the 3-m horn reflector. Pattern analysis produces the same curves as in Figure 8-21 except that cross-polarization in the horizontal plane is eliminated.

The design given in Figure 8-22 has $f = 9.8$ m, $D = 3$ m, $\theta_e = 20^\circ$, and tilts the subreflector axis by -73° to place the main reflector and subreflector in different quadrants. The Mizugutch criterion between the subreflector axis tilt and the feed tilt locates the feed axis at -97.5° relative to the main reflector axis and -24.5° relative to the subreflector axis. The parameters of the reflector were adjusted so that the plane wave radiated from the main reflector misses both the feed corrugated horn and the subreflector. All dimensions can be found using available equation sets [54] that require various sets of five inputs to totally specify the dual reflector. By using these equations, we discover that the hyperboloidal subreflector rim is an ellipse with 2.05- and 2.60-m diameters. To use the hyperbola close to the feed, specify a negative eccentricity and the equations curve the hyperbola toward the main reflector. Similarly, the equation for magnification produces a value of less than 1 for a negative eccentricity. Given the $e = -1.832$ for the reflector of Figure 8-22,

$$M = \frac{e + 1}{e - 1} = \frac{-1.832 + 1}{-1.832 - 1} = 0.2938$$

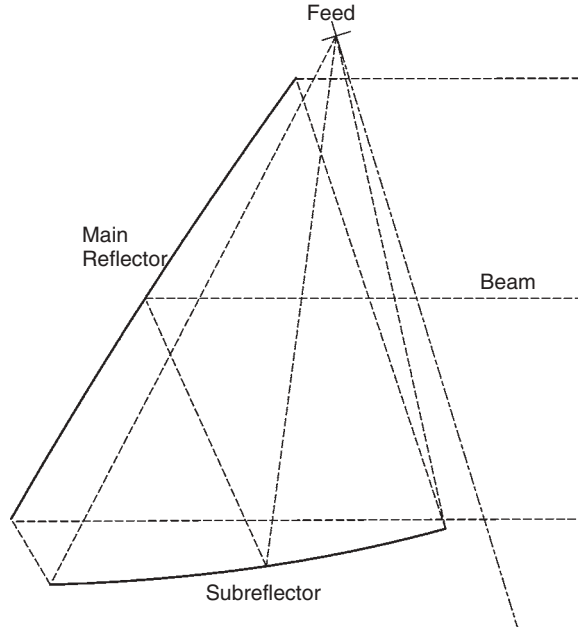


FIGURE 8-22 Dragonian dual-reflector geometry.

We compute feed tilt relative to the subreflector axis to satisfy the Mizugutch criterion:

$$\alpha = 2 \tan^{-1} \left(M \tan \frac{\beta}{2} \right) = 2 \tan^{-1} \left(0.2938 \tan \frac{-73}{2} \right) = -24.5^\circ$$

8-19 SPHERICAL REFLECTOR

When we feed-scan a paraboloidal reflector, the pattern sidelobes develop coma and the beam shape generally degrades. Feed scanning is limited. In a spherical reflector a feed moved in an arc from the center of the sphere and sees the same reflector geometry if we discount the edge effects. Greater scanning is possible, but the spherical reflector fails to focus an incident plane wave to a point and requires more elaborate feeds.

We can design many types of feeds for the spherical reflector. The reflector can be fed from a point source for large f/D by assuming that it is a distorted parabola [55,56]. It can be fed with a line source to follow the axis fields. Corrector subreflectors can be designed to correct the spherical aberrations [58]. Like the parabolic reflector, we can design arrays [24] to compensate for spherical aberrations and give multiple beams.

Figure 8-23 shows the geometry and ray tracing of a spherical reflector illuminated by a plane wave. All rays intersect a radial line of the sphere (the axis) in the direction of the incident wave because the reflector has circular symmetry about all axes. The diagram traces rays hitting the outer portion of the reflector as passing through the axis closer to the vertex than do the rays reflected from areas closer to the axis. The reflector has a line focus. A distorted paraboloidal reflector with a line focus exhibits spherical aberration because the focal length depends on the radial distance from the axis of the reflection point. The spherical reflector has a cusplike caustic where GO

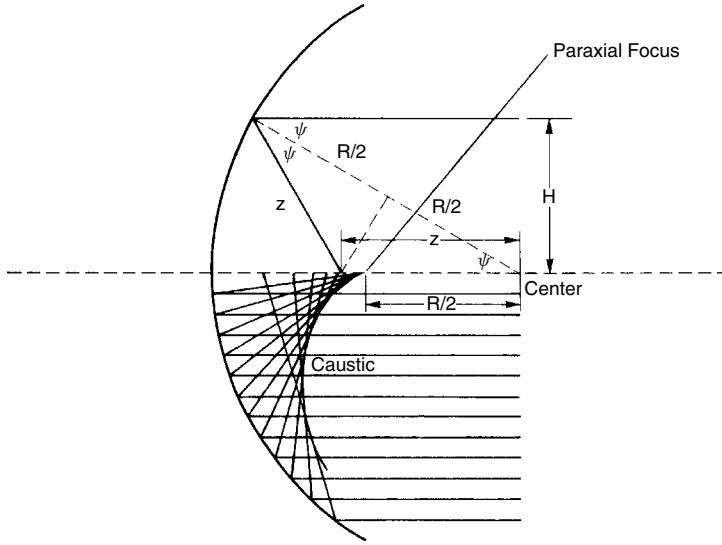


FIGURE 8-23 Ray tracing in a spherical reflector.

predicts infinite fields. The second side of Figure 8-23 traces a single ray. We can easily solve the isosceles triangle for the results:

$$z = \frac{R/2}{\sqrt{1 - H^2/R^2}} \quad (8-88)$$

$$H^2 = R^2 \left(1 - \frac{R^2}{4z^2} \right) \quad (8-89)$$

where z is the location of the focus for a given ray. As H approaches zero, with rays near the axis, the reflected ray passes through the paraxial focus ($z = R/2$).

We use Eq. (8-89) to find the power distribution on the axis by using the conservation of power. The power in a differential area of the plane wave reflects into a differential length on the axis: $dA = 2\pi H dH$. We differentiate Eq. (8-89) implicitly:

$$2H dH = \frac{R^2}{2z^3} dz$$

The power distribution along the axis is

$$P_z = \frac{P_0 R^3}{8z^3} \quad (8-90)$$

where P_0 is the power at the paraxial focus. The peak power occurs at the paraxial focus and drops by one-eighth (-9 dB) at the vertex. We determine the required length of the line source feed from the rotation angle ψ of the illuminated portion of the reflector:

$$\text{feed length} = \frac{R(1/\cos \psi - 1)}{2} \quad (8-91)$$

Example If the half-rotation angle of the illuminated region is 30° , the feed length is $0.0774R$ from Eq. (8-91). The amplitude decreases by

$$[\text{Eq. (8-90)}] \quad \frac{P_z}{P_0} = \frac{R^3}{8(R/2 + 0.0774R)^3} = 0.65 \quad (-1.9 \text{ dB})$$

The rays intersecting the axis are not at constant phase. The path length from the aperture plane through the reflector origin is

$$\text{path length} = \frac{R^2}{2z} + z \quad (8-92)$$

We can approximate Eq. (8-92) by a linear function if the feed length is short.

Example The feed length is $0.0774R$ long; calculate the phase change required along the feed.

The feed starts at the paraxial focus ($z = R/2$):

$$\text{path length} = \frac{R^2}{R} + \frac{R}{2} = 1.5R$$

At $z = R/2 + 0.0774R$, the path length $= 1.443R$. The phase change is $(2\pi/\lambda)R(0.0566)$. If we plot the phase change over the region of the feed, we can approximate the phase change by a linear function very accurately.

The spherical reflector can be fed from a point source when the f/D is large [55]. The center of the reflector approximates a parabola. The optimum focal point is

$$f = \frac{1}{4} \left[R + \sqrt{R^2 - (D/2)^2} \right] \quad (8-93)$$

The maximum phase path length error is [56]

$$\frac{\Delta L}{\lambda} = \frac{1}{2048} \frac{D}{\lambda} \frac{1}{(f/D)^3} \quad (8-94)$$

The approximate gain loss is

$$\frac{\Delta G}{G} = 3.5092 \left(\frac{\Delta L}{\lambda} \right)^2$$

or

$$\text{PEL(dB)} = 10 \log \left[1 - 3.5092 \left(\frac{\Delta L}{\lambda} \right)^2 \right] \quad (8-95)$$

A path length deviation of 0.25λ reduces the gain by 1.08 dB.

Example Determine the f/D value of a spherical reflector to limit ΔL to $1/16\lambda$ for a reflector diameter of 50λ .

By rearranging Eq. (8-94), we find that

$$\frac{f}{D} = \frac{16(50)}{2048} = 0.73$$

8-20 SHAPED REFLECTORS

Shaped reflectors spread cylindrical or spherical waves into a desired pattern that depends on geometric optics. Shaped reflectors do not radiate patterns exactly as prescribed by GO. In all cases we must apply techniques such as aperture diffraction, induced currents, or geometric theory of diffraction (GTD) to compute the actual pattern. We consider only the first-order GO for design, although analysis requires more elaborate techniques.

We use two principles to design shaped reflectors. The first is GO reflection expressed as a differential equation. The second is the conservation of power in ray tubes, which can be expressed either in terms of differential areas or integrals over sections of the feed and reflection patterns. We define two angles for the GO reflection equation. The feed points toward the reflector, and we measure its pattern angle ψ from an axis pointed toward the reflector. The reflector reradiates the incident feed pattern in a far-field pattern whose angle θ is measured from the axis pointing away from the reflector. The differential equation of reflection is [2]

$$\tan \frac{\theta + \psi}{2} = \frac{d\rho}{\rho d\psi} \quad (8-96)$$

where ρ is the distance of the reflector from the feed. The edges of the reflector are defined by angles ψ_1 and ψ_2 measured from the feed axis and reflect in directions θ_1 and θ_2 . We integrate this differential equation for a solution:

$$\ln \frac{\rho(\psi)}{\rho_0(\psi_1)} = \int_{\psi_1}^{\psi} \tan \frac{\theta(\psi) + \psi}{2} d\psi \quad (8-97)$$

where ψ_1 is some initial angle of the feed and $\rho(\psi_1)$ is the initial radius vector locating the reflector at ψ_1 .

GO, the zero-wavelength approximation, is consistent at any size. All parabolic reflectors collimate spherical waves radiated from the focus regardless of size. Only by considering diffraction or currents induced on the reflector can we compute gain and beamwidth of the antenna.

Example From Eq. (8-97), determine the reflector surface to give $\theta(\psi) = 0$.

$$\ln \frac{\rho(\psi)}{\rho_0(\psi_1)} = \int_{\psi_1}^{\psi} \tan \frac{\psi}{2} d\psi = -2 \left(\ln \cos \frac{\psi}{2} - \ln \cos \frac{\psi_1}{2} \right)$$

By the properties of the \ln function, this becomes

$$\ln \frac{\rho(\psi)}{\rho_0(\psi_1)} = \ln \frac{\cos^2(\psi_1/2)}{\cos^2(\psi/2)}$$

By taking the exponential of each side, we get the polar equation of the reflector:

$$\rho(\psi) = \rho_0(\psi_1) \frac{\cos^2(\psi_1/2)}{\cos^2(\psi/2)}$$

We let $\psi_1 = 0$ and set $\rho(\psi) = f$, and we obtain the equation for the parabola [Eq. (8-1)].

The differential equation of reflection tells us only the shape of the reflector locally to produce a reflection in a direction θ for an incident angle ψ . We must still find the power density in various directions. The ratio of differential areas gives us these power densities. Given the pattern of the feed $G_f(\psi, \phi)$ and the pattern of the reflection $P(\theta, \phi)$,

$$KP(\theta, \phi) dA(\theta, \phi) = G_f(\psi, \phi) dA_f(\psi, \phi) \quad (8-98)$$

where $dA(\theta, \phi)$ is the differential area of the reflection pattern, $dA_f(\psi, \phi)$ the differential area of the feed pattern, and K a constant found by equating the total incident and reflected powers. Equation (8-98) is based on the assumption that reflections are 1:1 with the feed pattern.

8-20.1 Cylindrical Reflector Synthesis

We feed cylindrical reflectors with line sources. The reflector determines the beam shape in one plane and the line-source distribution in the other. The problem reduces to designing a single two-dimensional curve moved along an axis to define the reflector. The power radiated by the feed is given by $G_f(\psi) d\psi$. The reflector directs this power at an angle θ whose power density is $P(\theta) d\theta$. These are proportional [Eq. (8-98)]:

$$KP(\theta) d\theta = G_f(\psi) d\psi \quad (8-99)$$

At the limits of the reflector, feed angles ψ_1 and ψ_2 reflect to angles θ_1 and θ_2 . We calculate the constant K by equating the power in each pattern:

$$K = \frac{\int_{\psi_1}^{\psi_2} G_f(\psi) d\psi}{\int_{\theta_1}^{\theta_2} P(\theta) d\theta} \quad (8-100)$$

We integrate Eq. (8-99) to derive a formal solution usually arrived at numerically. By combining Eqs. (8-99) and (8-100), we eliminate K :

$$\frac{\int_{\theta_1}^{\theta} P(\theta) d\theta}{\int_{\theta_1}^{\theta_2} P(\theta) d\theta} = \frac{\int_{\psi_1}^{\psi} G_f(\psi) d\psi}{\int_{\psi_1}^{\psi_2} G_f(\psi) d\psi} \quad (8-101)$$

We use Eq. (8-101) with a known feed pattern $G_f(\psi)$ and a desired pattern function $P(\theta)$ to establish the relation $\theta(\psi)$. We insert $\theta(\psi)$ into the differential equation for

the reflection [Eq. (8-97)] and determine radial distance as a function of ψ :

$$\rho(\psi) = \rho_0(\psi_1) \exp \left[\int_{\psi_1}^{\psi} \tan \frac{\theta(\psi) + \psi}{2} d\psi \right] \quad (8-102)$$

With Eq. (8-102) we calculate the reflector coordinates to within a scale factor $\rho_0(\psi_1)$.

8-20.2 Circularly Symmetrical Reflector Synthesis

The synthesis of circularly symmetrical reflectors is readily reduced to a two-dimensional problem. We must assume that the feed pattern is also axisymmetrical. We describe the feed pattern by $G_f(\psi)$ and the reflector pattern by $P(\theta)$. The differential areas are $\sin \psi d\psi$ and $\sin \theta d\theta$. Equation (8-98) becomes

$$KP(\theta) \sin \theta d\theta = G_f(\psi) \sin \psi d\psi \quad (8-103)$$

We integrate Eq. (8-103) to find the function $\theta(\psi)$:

$$\frac{\int_{\theta_1}^{\theta} P(\theta) \sin \theta d\theta}{\int_{\theta_1}^{\theta_2} P(\theta) \sin \theta d\theta} = \frac{\int_{\psi_1}^{\psi} G_f(\psi) \sin \psi d\psi}{\int_{\psi_1}^{\psi_2} G_f(\psi) \sin \psi d\psi} \quad (8-104)$$

We use Eq. (8-102) from the reflection differential equation with $\theta(\psi)$ to determine the polar equation of the reflector. The design of a shaped reflector can best be explained with an example. The cylindrical reflector synthesis follows parallel steps.

Example Design a reflector to transform the feed pattern of Figure 8-24a into the pattern of Figure 8-24b.

The required pattern drops by about 9 dB from 50° to 0° . We will use the feed pattern from 4° to 54° and design a reflector with a ring caustic. The feed pattern at 4° is reflected to 50° , and the feed pattern at 54° is reflected to 0° . The geometric optics rays cross somewhere in front of the reflector. We have the following limits:

$$\text{Feed: } \psi_1 = 4^\circ, \psi_2 = 54^\circ$$

$$\text{Reflection: } \theta_1 = 50^\circ, \theta_2 = 0$$

We insert the patterns of Figure 8-24 into both sides of Eq. (8-104) and evaluate the ratio of the integrals. Table 8-12 gives the results of these integrals for θ and ψ as normalized in Eq. (8-104). Given ψ , we find θ by equating integrals in the table. For example, follow the line from $\psi = 28^\circ$ (feed) to its integral value, match the values of the integrals, and determine the reflection angle $\theta = 42^\circ$. We trace a number of these through interpolation to generate Table 8-13 of reflection angles $\theta(\psi)$ for given feed angles.

We use Table 8-13 of $\theta(\psi)$ in the integral of Eq. (8-102) to calculate the normalized polar equation of the reflector listed in Table 8-14. Figure 8-25 shows the reflector shape as well as the geometry of axisymmetric-shaped reflectors. There is a hole in the center because the procedure fails to specify that region. Note in Table 8-12 how

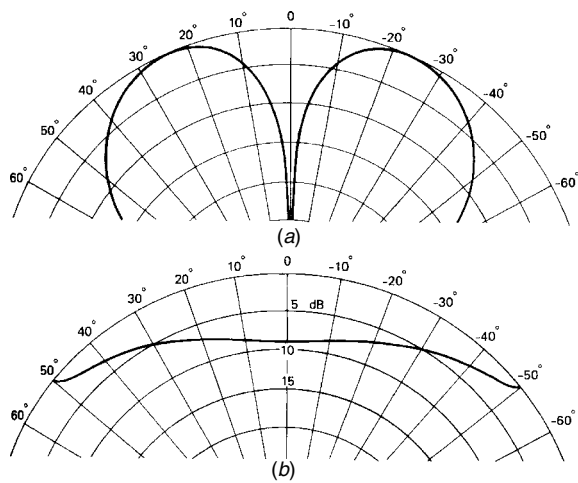


FIGURE 8-24 Axisymmetrical reflector pattern transformation: (a) feed pattern; (b) reflector pattern.

TABLE 8-12 Use of Normalized Integrals of Feed and Pattern Power to Determine $\theta(\psi)$ in Shaped Reflector Synthesis

Feed Angle, ψ (deg)	Feed Normalized Integral	Reflection Normalized Integral	Reflection Angle, θ (deg)
4	0.000	0.000	50
6	0.002	0.143	48
8	0.006	0.259	46
10	0.016	0.360	44
12	0.031	0.449	42
14	0.054	0.527	40
16	0.086	0.596	38
18	0.128	0.657	36
20	0.178	0.711	34
22	0.237	0.757	32
24	0.302	0.798	30
26	0.373	0.833	28
28	0.445	0.864	26
30	0.518	0.889	24
32	0.590	0.911	22
34	0.658	0.930	20
36	0.720	0.946	18
38	0.777	0.959	16
40	0.827	0.970	14
42	0.869	0.978	12
44	0.905	0.985	10
46	0.934	0.991	8
48	0.958	0.995	6
50	0.976	0.998	4
52	0.999	0.999	2
54	1.000	1.000	0

TABLE 8-13 Shaped Reflector Synthesis Reflection Angles for Given Feed Angles, $\theta(\psi)$

Feed Angle, ψ (deg)	Reflection Angle, θ (deg)	Feed Angle, ψ (deg)	Reflection Angle, θ (deg)
4	50.0	30	40.2
6	50.0	32	38.2
8	49.9	34	36.0
10	49.8	36	33.6
12	49.6	38	31.1
14	49.3	40	28.4
16	48.8	42	25.6
18	48.2	44	22.6
20	47.4	46	19.5
22	46.4	48	16.2
24	45.2	50	12.6
26	43.7	52	8.4
28	42.1	54	0.0

TABLE 8-14 Shaped Reflector Synthesis Normalized Polar Equation of a Reflector, $\rho(\psi)$

Feed Angle, ψ (deg)	Normalized Radius, ρ	Feed Angle, ψ (deg)	Normalized Radius, ρ	Feed Angle, ψ (deg)	Normalized Radius, ρ
4	1.000	22	1.208	40	1.503
6	1.018	24	1.238	42	1.539
8	1.038	26	1.268	44	1.575
10	1.058	28	1.299	46	1.611
12	1.080	30	1.332	48	1.648
14	1.103	32	1.365	50	1.684
16	1.128	34	1.398	52	1.719
18	1.153	36	1.433	54	1.753
20	1.180	38	1.468		

much of the inner portion of the reflector must reflect rays near 50° to achieve the high gain required. We could repeat the example and design without a ring caustic where rays from the feed near 54° reflect to 50° and would produce a flatter reflector.

Because diffraction effects spread the pattern, we could approximate the pattern of Figure 8-24*b* by designing a reflector to point the beam in a cone about the axis. If we take Eq. (8-97) and let $\theta(\psi) = \theta_0$, a constant, we get the surface

$$\rho(\psi) = \rho_0 \frac{\cos^2[(\psi_0 + \theta_0)/2]}{\cos^2[(\psi + \theta_0)/2]} \quad (8-105)$$

Example Estimate the directivity of a 40λ -diameter reflector shaped by Eq. (8-105) to scan in a cone to $\theta_0 = 50^\circ$.

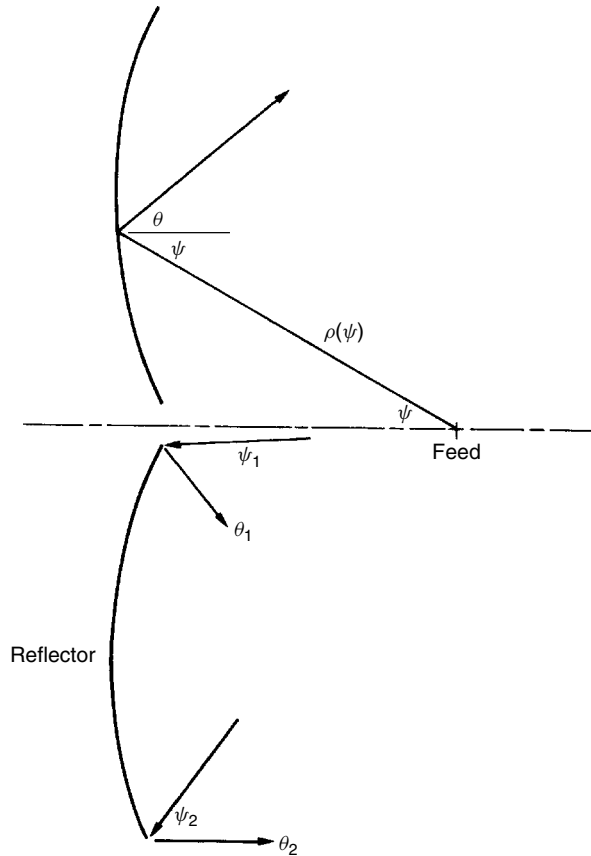


FIGURE 8-25 Circularly symmetrical reflector designed with a caustic reflector.

Only half of the diameter is used for each side. The effective scanned aperture width becomes $(40\lambda/2) \cos 50^\circ = 12.8\lambda$. If we assume a uniform-amplitude aperture distribution, we obtain an upper bound. From Eq. (4-83), $\text{HPBW} = 59^\circ/12.8 = 4.6^\circ$. We use Eq. (1-24) to estimate the directivity:

$$\text{directivity} = \frac{2}{\cos(50^\circ - 2.3^\circ) - \cos(50^\circ + 2.3^\circ)} = 32.5 \quad (15 \text{ dB})$$

The boresight gain of the aperture with a uniform distribution is 42 dB. Spreading the reflection into a cone greatly reduces gain. The shaped reflector above will have even less directivity because it has a greater edge taper.

8-20.3 Doubly Curved Reflector for Shaped Beams

It is a common radar requirement to have a narrow beam in one plane and a shaped beam in the other. Such beams can be obtained from shaped cylindrical reflectors, but it is simpler to replace the line source with a single feed. We only specify the pattern in the principal planes denoted: θ_V , the shaped pattern coordinate, and θ_H , the pencil

beam [2,59]. Similarly, we specify the feed antenna pattern in terms of ψ_V and ψ_H . For a given feed angle ψ_V , the reflected wave angle is θ_V . The only θ_H value allowed is zero. The reflector collimates the wave in the horizontal plane. This collimation requires a symmetrical reflector made from parabolic curves in the horizontal plane. We design the vertical curve only through the center of the reflector.

For a given feed angle ψ_V (Figure 8-26a), all incoming rays at an angle θ_V must be reflected into the feed. The incoming rays form the $x-z'$ plane in Figure 8-26, and the reflector collimates these to the feed by a parabola in the plane. We call this parabola a *rib* of the reflector. Figure 8-26b shows the plane and two rays reflecting into the feed from a wave arriving at an angle θ_V in the $x-z'$ plane. For the beam to focus, the optical path lengths must be equal:

$$\overline{BP} + \overline{PO} = \overline{AN} + \overline{NO} \quad (8-106)$$

Equation (8-106) establishes the curve of the rib in the $x-z'$ plane as a parabola with focal length

$$f = \rho_c(\psi_V) \cos^2 \frac{\theta_V(\psi_V) + \psi_V}{2} \quad (8-107)$$

with the focus located on the z' -axis. Using the parabolic ribs reduces the problem to the design of the central curve $\rho_c(\psi_V)$.

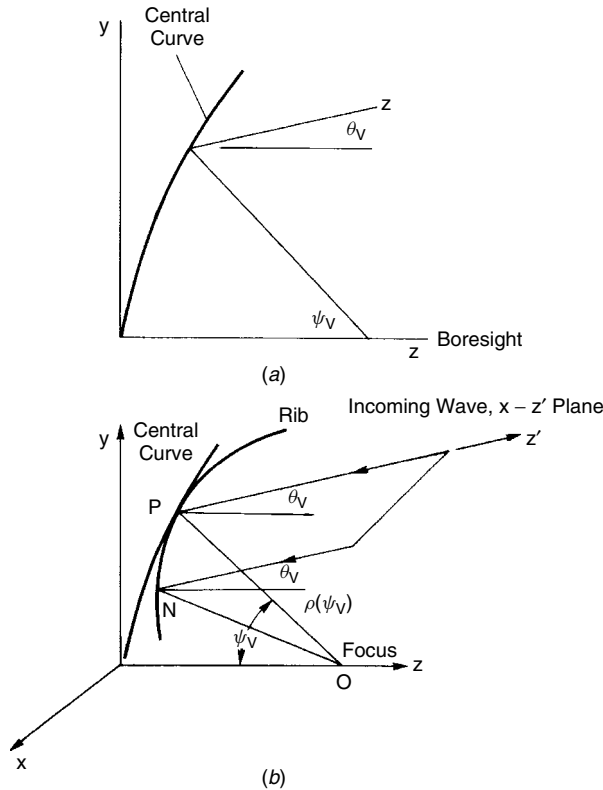


FIGURE 8-26 Doubly curved shaped reflector.

The reflected and feed power densities modify Eq. (8-98) to

$$K P(\theta_V) d\theta_V \rho_c(\psi_V) d\psi_V = G_f(\psi_V) d\psi_V d\psi_H \quad (8-108)$$

We integrate Eq. (8-108) and normalize to the total power:

$$\frac{\int_{\theta_1}^{\theta_2} P(\theta_V) d\theta_V}{\int_{\theta_1}^{\theta_2} P(\theta_V) d\theta_V} = \frac{\int_{\psi_1}^{\psi_2} [G_f(\psi_V)/\rho_c(\psi_V)] d\psi_V}{\int_{\psi_1}^{\psi_2} [G_f(\psi_V)/\rho_c(\psi_V)] d\psi_V} \quad (8-109)$$

Equation (8-109) is similar to Eqs. (8-101) and (8-104) except that the feed pattern integral value depends on the radial distance to the central rib. We must know $\rho_c(\psi_V)$ before we can determine $\theta_V(\psi_V)$, which will be required to compute $\rho_c(\psi_V)$ from the reflection differential equation [Eq. (8-102)]. The solution can be found only by an iterative process.

We must assume a $\rho_c(\psi_V)$, solve for $\theta_V(\psi_V)$, and use the result to compute a new $\rho_c(\psi_V)$. After a few iterations, the values of $\rho_c(\psi_V)$ converge. We use the normalized ρ_c with the foregoing ratio of integrals. We start with a parabola:

$$\frac{\rho_c(\psi_V)}{\rho_c(\psi_1)} = \frac{\cos^2(\psi_1/2)}{\cos^2(\psi_V/2)}$$

The surface generated by following the method may not be defined uniquely. We pick a constant width for the reflector in the horizontal plane. We define the surface with a continuous series of parabolas each in a $x-z'$ plane determined by the reflection angle θ_V , which changes direction along the central rib. We must plot the curve of the vertical coordinate of the edge versus ψ_V to see if it is monotonic. If there are loops in the curve, the surface defined is not unique.

Given the width x , we calculate the vertical coordinate of the edge by the following development. The location of the rib on the central curve is given by $\rho_c(\psi_V) \sin \psi_V$. The rib is a parabola in the $x-z'$ plane with its focus given by Eq. (8-107). The z' -coordinate at the edge is $z' = x^2/4f(\psi_V)$. We determine the vertical dimension by projecting this point onto the y -axis: $y = \rho_c(\psi_V) \sin \psi_V$. Elliott [60, p. 500] points out that by following this method, one does not get the proper slope for reflection at all points, but we will get the desired pattern when we design for only small deviations from a pencil beam. The surface can be designed with or without a caustic depending on the reflection angles at the edges. Reflectors designed with caustic edge reflections have a better chance of being unique [60]. Carberry [61] presents a method of analysis that involves physical optics. When we apply these methods, we must subdivide the reflector into many patches because the phases of the currents change rapidly with position on the reflector, and the analysis must be repeated with finer and finer patches until the result converges.

8-20.4 Dual Shaped Reflectors

We can design a dual-reflector antenna to produce an arbitrary phase and amplitude in the aperture plane by shaping both reflectors. By using both the conservation of power

and the differential equations of reflection on the two surfaces, Galindo [62] derived a pair of differential equations in terms of the aperture radius. Runge–Kutta or any other suitable numerical method can be used to solve the simultaneous differential equations instead of an integration of the power equation. Williams [63] finds a solution to Cassegrain antennas within the restriction of equal amplitude and phase in the aperture plane by integration of the power equation. Collins [64] considers using a parabolic reflector for the main reflector, since the difference between the shaped main reflector and a parabola is small. He accepts a quadratic phase error in the aperture. Existing large reflectors can be retrofitted with a shaped subreflector to improve performance. For the method to work, an axisymmetric feed such as a corrugated horn is required.

Galindo-Israel and Mittra [65] use a pair of reflectors offset from each other to transform a spherical wave from a feed antenna into a second spherical wave with a modified pattern amplitude. This combination of a feed with two reflectors can illuminate either prime focus paraboloidal reflectors or Cassegrain systems without modification of the existing reflector surfaces. For example, a $\sec^4(\theta/2)$ pattern can be realized from an ordinary pattern source to increase the aperture efficiency of the overall reflector system. The reflectors maintain equal GO path lengths for all rays, but they only approximate the desired pattern amplitude from the virtual focus. The procedure can be used to determine the contours of the reflectors along radial lines through numerical solution of differential equations. The equations develop from simplifying assumptions that depend on the extra degree of freedom introduced by the second reflector. In most cases, solution of the equations produces usable designs, although the method is not exact.

Lee et al. [66] developed a method to shape offset-fed dual reflectors that reduces to the solution of a differential equation similar to that of the single-reflector design given above. The reflection properties of the subreflector determine the main reflector amplitude distribution to first order. This method does not produce exact results but is close enough for engineering purposes. We start with a desired aperture power distribution $P(r, \phi_c)$ and a known feed power pattern $G_f(\theta', \phi_c)$ given in the radial direction ϕ_c . Most cases use distributions independent of ϕ_c , but the design is performed along these planes. For a circularly symmetric design we only need to solve the differential equation along one plane, but the general case requires solutions along enough planes to allow splines along the coordinate ϕ_c to find every point on both reflectors.

A differential expression relates the feed power to the aperture power:

$$G_f(\theta', \phi_c) \sin \theta' d\theta' = P(r, \phi_c) r dr$$

This leads to a ratio of integrals:

$$\frac{\int_{-\theta_e}^{\theta} G_f(\theta') \sin \theta' d\theta'}{\int_{-\theta_e}^{\theta_e} G_f(\theta') \sin \theta' d\theta'} = \frac{\int_{R_1}^R P(r') r' dr'}{\int_{R_1}^{R_2} P(r') r' dr'} \quad (8-110)$$

Equation (8-110) covers the general case where the offset subreflector directs power from a lower angle $-\theta_e$ to an offset radius R_1 that changes for each plane ϕ_c . For a circularly symmetric design, $-\theta_e = 0$ and $R_1 = 0$. Although many designs attempt to generate a uniform aperture distribution for the main reflector, we can substitute

any distribution, such as a circular Taylor distribution to control the sidelobes into Eq. (8-110). Given the aperture distribution and the feed pattern, we calculate a table similar to Table 8-12 for each plane ϕ_c that gives the feed angle as a function of aperture radius. We interpolate on this table to determine every value.

We start at the center of the subreflector described in spherical coordinates $(\rho_0, 0, 0)$ relative to the axis of the subreflector centered at the feed focus. The subreflector axis may be tilted relative to the main reflector axis. The rectangular coordinates of the subreflector are $(\rho \sin \theta \cos \phi_c, \rho \sin \theta \sin \phi_c, \rho \cos \theta)$. The incident wave reflects to a point on the main reflector: $(H \pm R \cos \phi_c, \pm R \sin \phi_c, z)$ using + Cassegrain, –Gregorian. We calculate the unit vector between the subreflector point and the main reflector. The normal vector on the subreflector is expressed as a differential:

$$\mathbf{n} = \frac{1}{\Delta} \left(\mathbf{a}_\rho - \frac{1}{\rho} \frac{\partial \rho}{\partial \theta} \mathbf{a}_\theta - \frac{1}{\rho \sin \theta} \frac{\partial \rho}{\partial \phi_c} \mathbf{a}_{\phi_c} \right) \quad (8-111)$$

where

$$\Delta = \sqrt{1 + \left(\frac{1}{\rho} \frac{\partial \rho}{\partial \theta} \right)^2 + \left(\frac{1}{\rho \sin \theta} \frac{\partial \rho}{\partial \phi_c} \right)^2}$$

We apply both equations of Snell's law [Eq. (2-67)] to the subreflector reflection and gather terms to form a pair of differential equations:

$$\frac{\partial \rho}{\partial \theta} = \frac{QV}{Q^2 + U^2} \quad \text{and} \quad \frac{\partial \rho}{\partial \phi_c} = \frac{UV \sin \theta}{Q^2 + U^2} \quad (8-112)$$

The terms of Eq. (8-112) are given by the expressions

$$\begin{aligned} Q &= \frac{a \cos \theta \cos \phi_c + b \sin \theta \sin \phi_c - c \sin \theta}{\rho} \\ U &= \frac{b \cos \phi_c - a \sin \phi_c}{\rho} \\ V &= L + a \sin \theta \cos \phi_c + b \sin \theta \sin \phi_c + c \sin \theta \\ a &= H \pm R \cos \phi_c - \rho \sin \theta \cos \phi_c \\ b &= \pm R \sin \phi_c - \rho \sin \theta \sin \phi_c \\ c &= z - \rho \cos \theta \end{aligned} \quad (8-113)$$

where the vector (a, b, c) is from the subreflector to the main reflector and $L = \sqrt{a^2 + b^2 + c^2}$.

We choose $z = 0$ as the aperture and equate path lengths along every ray. This gives an equation for the z -position of the main reflector:

$$\overline{OL} = \rho_0 + L_0 - z_0 = \rho + L - z$$

We solve for z :

$$z = \frac{a^2 + b^2}{2(\rho \cos \theta - \rho + \overline{OL})} + \frac{1}{2}(\rho \cos \theta - \rho + \overline{OL}) \quad (8-114)$$

To solve for the reflector surfaces, we choose a starting point, usually the center of the reflector as the first ray from the feed to the subreflector, and calculate the initial distance L_0 between the subreflector and the main reflector to find the path length. We select a polar plane ϕ_c and solve the left differential equation [Eq. (8-112)] for both surfaces using a Runge–Kutta numerical solution. We repeat this in a sufficient number of planes ϕ_c to specify the surface totally. If the antenna is circularly symmetric, we solve the equation only once. For an offset dual reflector we can improve the cross-polarization by computing an equivalent subreflector using least squares and use its eccentricity to calculate the Mizugutch subreflector axis rotation.

8-21 OPTIMIZATION SYNTHESIS OF SHAPED AND MULTIPLE-BEAM REFLECTORS

Silver [2] discusses using a linear array feed to shape the beam of a paraboloidal reflector. The method is quite empirical and involves the addition of a number of offset beams. A similar technique is used in three-dimensional radar, but the feeds are kept separate so that multiple beams can scan a larger area in a given time. An array feed provides the best solution to beam shaping in many cases. The number of elements in the array limits the number of variables to a finite set to which optimization techniques can be applied.

A second method uses optimization to shape the reflector and possible subreflectors. This requires distortion functions on the reflectors. We start with conic-section reflectors and add distortions. These distortions can be global Zernike functions defined over the total surface, or they could be localized functions such as B -splines [67]. A B -spline uses a grid of points on the reflector, but the spline coefficients apply only over a limited area. In both cases we obtain a set of coefficients used in the optimization algorithms. We have the choice of combining these coefficients, or we can iterate between different sets of coefficients. Optimization is an art.

Because the reflector is an aperture antenna, we pick a set of directions in $(u, v) = (\sin \theta \cos \phi, \sin \theta \sin \phi)$ space to evaluate the pattern. The number of points should exceed the number of coefficients and be spaced close enough to fully describe the main-beam pattern:

$$\Delta u \text{ and } \Delta v \sim \frac{0.5\lambda}{D} \text{ to } \frac{0.25\lambda}{D} \quad (8-115)$$

We calculate the pattern power $P_m(u, v)$ at these points and compare them to the desired pattern $P_m^d(u, v)$ using a suitable cost function. We weight each pattern direction ω_m and use a summation cost [68] with a gradient minimization technique:

$$F(\mathbf{x}) = \sum_{m=1}^M |\omega_m(P_m(u_m, v_m)) - P_m^d(u_m, v_m)|^2 \quad (8-116)$$

A second choice is a min–max optimization [69]. This algorithm minimizes the maximum error:

$$\max[\omega_m(P_m(u_m, v_m)) - P_m^d(u_m, v_m)] \quad (8-117)$$

If we optimize the reflector shape, we express the distortion as B -splines specified at evenly spaced points across the aperture with the number determined by the maximum pattern angle θ_{\max} and the reflector diameter D [69]:

$$N_x = N_y = \frac{\pi D \sin \theta_{\max}}{\lambda} + 2 \quad (8-118)$$

Given a Zernike polynomial expansion with maximum azimuthal mode expansion M_{\max} and maximum polar mode index N_{\max} , we have similar mode number requirements:

$$M_{\max} = N_{\max} = \frac{\pi D \sin \theta_{\max}}{\lambda} + 2 \quad (8-119)$$

Shaping starts with a paraboloid main reflector whose beamwidth may be so narrow that a portion of the specified $u-v$ space area may lie in the sidelobe region. In this case the optimization may become trapped because it cannot satisfy this area when changes effecting the main beam region positively affect the sidelobe region negatively. We must distort the main reflector before starting the optimization [69]. First surround the $u-v$ space area of specified points with an ellipse centered at (u_0, v_0) with major radius ω_1 and minor radius ω_2 tilted an angle α . Given a paraboloid with diameter D , focal length f , and center offset (x_0, y_0) , we define rotated coordinates on the aperture.

$$\begin{aligned} x' &= (x - x_0) \cos \alpha + (y - y_0) \sin \alpha \\ y' &= -(x - x_0) \sin \alpha + (y - y_0) \cos \alpha \end{aligned}$$

Using these coordinates, we alter the z -axis position of the reflector:

$$\Delta z = - \left(\frac{1}{2} + \frac{x^2 + y^2}{8f^2} \right) \left[\frac{\omega_1 x'^2 + \omega_2 y'^2}{D} + u_0(x - x_0) + v_0(y - y_0) \right] \quad (8-120)$$

We have a choice with ω_1 and ω_2 because they can be both either positive or negative. Positive values flatten the reflector while negative values cause a caustic reflection to broaden the beam.

REFERENCES

1. A. W. Love, *Reflector Antennas*, IEEE Press, New York, 1978.
2. S. Silver, ed., *Microwave Antenna Theory and Design*, McGraw-Hill, New York, 1949.
3. W. V. T. Rusch and P. D. Potter, *Analysis of Reflector Antennas*, Academic Press, New York, 1970.
4. P. J. Wood, *Reflector Antenna Analysis and Design*, Peter Peregrinus, London, 1980.
5. C. A. Mentzer and L. Peters, A GTD analysis of the far-out sidelobes of Cassegrain antennas, *IEEE Transactions on Antennas and Propagation*, vol. AP-23, no. 5, September 1975, pp. 702–709.
6. S. W. Lee et al., Diffraction by an arbitrary subreflector: GTD solution, *IEEE Transactions on Antennas and Propagation*, vol. AP-27, no. 3, May 1979, pp. 305–316.
7. A. D. Craig and P. D. Simms, Fast integration techniques for reflector antenna pattern analysis, *Electronics Letters*, vol. 18, no. 2, January 21, 1982, pp. 60–62.

8. V. Galindo-Israel and R. Mittra, A new series representation for the radiation integral with application to reflector antennas, *IEEE Transactions on Antennas and Propagation*, vol. AP-25, no. 5, September 1977, pp. 631–641.
9. A. W. Rudge et al., eds., *The Handbook of Antenna Design*, Vol. 1, Peter Peregrinus, London, 1982.
10. A. C. Ludwig, The definition of cross polarization, *IEEE Transactions on Antennas and Propagation*, vol. AP-21, no. 1, January 1973, pp. 116–119.
11. J. R. Cogdell and J. H. Davis, Astigmatism in reflector antennas, *IEEE Transactions on Antennas and Propagation*, vol. AP-21, no. 4, July 1973, pp. 565–567.
12. Y. T. Lo, On the beam deviation factor of a parabolic reflector, *IEEE Transactions on Antennas and Propagation*, vol. AP-8, no. 3, May 1960, pp. 347–349.
13. J. Ruze, Lateral-feed displacement in a paraboloid, *IEEE Transactions on Antennas and Propagation*, vol. AP-13, no. 5, September 1965, pp. 660–665.
14. W. V. T. Rusch and A. C. Ludwig, Determination of the maximum scan-gain contours of a beam scanned paraboloid and their relation to the Petzval surface, *IEEE Transactions on Antennas and Propagation*, vol. AP-21, no. 2, March 1973, pp. 141–147.
15. W. A. Imbriale, P. G. Ingerson, and W. C. Wong, Large lateral feed displacements in a parabolic reflector, *IEEE Transactions on Antennas and Propagation*, vol. AP-22, no. 6, November 1974, pp. 742–745.
16. D. K. Cheng, Effect of arbitrary phase errors on the gain and beamwidth characteristics of radiation pattern, *IEEE Transactions on Antennas and Propagation*, vol. AP-3, no. 4, July 1955, pp. 145–147.
17. J. Ruze, Antenna tolerance theory: a review, *Proceedings of IRE*, vol. 54, no. 4, April 1966, pp. 633–640.
18. M. S. Zarghamee, On antenna tolerance theory, *IEEE Transactions on Antennas and Propagation*, vol. AP-15, no. 6, November 1967, pp. 777–781.
19. R. C. Hansen, ed., *Microwave Scanning Antennas*, Academic Press, New York, 1964.
20. W. V. T. Rusch and R. D. Wanselow, Boresight gain loss and gore related sidelobes of an umbrella reflector, *IEEE Transactions on Antennas and Propagation*, vol. AP-30, no. 1, January 1982, pp. 153–157.
21. W. H. Watson, The field distribution in the focal plane of a paraboloidal reflector, *IEEE Transactions on Antennas and Propagation*, vol. AP-12, no. 5, September 1964, pp. 561–569.
22. T. B. Vu, Optimization of efficiency of reflector antennas: approximate method, *Proceedings of IEE*, vol. 117, January 1970, pp. 30–34.
23. B. M. Thomas, Theoretical performance of prime focus paraboloids using cylindrical hybrid modes, *Proceedings of IEE*, vol. 118, November 1971, pp. 1539–1549.
24. N. Amitay and H. Zucker, Compensation of spherical reflector aberrations by planar array feeds, *IEEE Transactions on Antennas and Propagation*, vol. AP-20, no. 1, January 1972, pp. 49–56.
25. V. Galindo-Israel, S. W. Lee, and R. Mittra, Synthesis of laterally displaced cluster feed for a reflector antenna with application to multiple beams and contoured patterns, *IEEE Transactions on Antennas and Propagation*, vol. AP-26, no. 2, March 1978, pp. 220–228.
26. B. Popovich et al., Synthesis of an aberration corrected feed array for spherical reflector antennas, *IEEE/APS Symposium Digest*, May 1983.
27. V. Mrstik, Effect of phase and amplitude quantization errors on hybrid phased-array reflector antennas, *IEEE Transactions on Antennas and Propagation*, vol. AP-30, no. 6, November 1982, pp. 1233–1236.
28. C. M. Knop, On the front to back ratio of a parabolic dish antenna, *IEEE Transactions on Antennas and Propagation*, vol. AP-24, no. 1, January 1976, pp. 109–111.

29. M. Uhm, A. Shishlov, and K. Park, Offset-paraboloid geometry: relations for practical use, *IEEE Antennas and Propagation Magazine*, vol. 38, no. 3, June 1996, pp. 77–79.
30. R. F. H. Yang, Illuminating curved passive reflector with defocused parabolic antenna, *1958 IRE Wescon Convention Record*, August 1958, pp. 260–265.
31. C. Granet, Designing axially symmetric Cassegrain and Gregorian dual-reflector antennas from combinations of prescribed geometric parameters, *IEEE Antennas and Propagation Magazine*, vol. 40, no. 2, April 1998, pp. 76–82.
32. C. Granet, Designing axially symmetric Cassegrain and Gregorian dual-reflector antennas from combinations of prescribed geometric parameters, part 2: minimum blockage condition while taking into account the phase-center of the feed, *IEEE Antennas and Propagation Magazine*, vol. 40, no. 3, June 1998, pp. 82–85.
33. W. V. T. Rusch, Phase error and associated cross polarization effects in Cassegrainian-fed microwave antennas, *IEEE Transactions on Antennas and Propagation*, vol. AP-14, no. 3, May 1966, pp. 266–275.
34. P.-S. Kildal, The effects of subreflector diffraction on the aperture efficiency of a conventional Cassegrain antenna: an analytical approach, *IEEE Transactions on Antennas and Propagation*, vol. AP-31, no. 6, November 1983, pp. 903–909.
35. A. M. Isber, Obtaining beam-pointing accuracy with Cassegrain antennas, *Microwaves*, August 1967, pp. 40–44.
36. W. V. T. Rusch and R. Wohlleben, Surface tolerance loss for dual-reflector antennas, *IEEE Transactions on Antennas and Propagation*, vol. AP-30, no. 4, July 1982, pp. 784–785.
37. A. F. Kay, Electrical design of metal space frame radomes, *IEEE Transactions on Antennas and Propagation*, vol. AP-13, no. 2, March 1965, pp. 188–202.
38. P.-S. Kildal, E. Olsen, and J. A. Aas, Losses, sidelobes, and cross polarization caused by feed-support struts in reflector antennas: design curves, *IEEE Transactions on Antennas and Propagation*, vol. AP-36, no. 2, February 1988, pp. 182–190.
39. W. V. T. Rusch et al., Forward scattering from square cylinders in the resonance region with application to aperture blockage, *IEEE Transactions on Antennas and Propagation*, vol. AP-24, no. 2, March 1976, pp. 182–189.
40. G. T. Ruck, ed., *Radar Cross Section Handbook*, Vol. 1, Plenum Press, New York, 1970.
41. G. W. Collins, Noise temperature calculations from feed system characteristics, *Microwave Journal*, vol. 12, December 1969, pp. 67–69.
42. B. E. Kinber, On two-reflector antennas, *Radioengineering and Electronics*, vol. 7, no. 6, 1962, pp. 973–980.
43. A. P. Popov and T. A. Milligan, Amplitude aperture-distribution control in displaced-axis two reflector antennas, *IEEE Antennas and Propagation Magazine*, vol. 39, no. 6, December 1997, pp. 58–63.
44. S. P. Morgan, Some examples of generalized Cassegrainian and Gregorian antennas, *IEEE Transactions on Antennas and Propagation*, vol. AP-12, no. 6, November 1964, pp. 685–691.
45. C. Granet, A simple procedure for the design of classical displaced-axis dual-reflector antennas using a set of geometric parameters, *IEEE Antennas and Propagation Magazine*, vol. 41, no. 6, December 1999, pp. 64–72.
46. T. A. Milligan, The effects of feed movement on the displaced-axis dual reflector, *IEEE Antennas and Propagation Magazine*, vol. 40, no. 3, June 1998, pp. 86–87.
47. Y. Mizugutch, M. Akagawa, and H. Yokoi, Offset dual reflector antenna, *IEEE Symposium on Antennas and Propagation Digest*, 1976, pp. 2–5.
48. P. H. Nielson and S. B. Sørensen, *Grasp8 Software Users Manual*, Ticra, Copenhagen, 2001.

49. C. Granet, Designing classical offset Cassegrain or Gregorian dual-reflector antennas from combinations of prescribed geometric parameters, *IEEE Antennas and Propagation Magazine*, vol. 44, no. 3, June 2002, pp. 114–123.
50. C. Granet, Designing classical offset Cassegrain or Gregorian dual-reflector antennas from combinations of prescribed geometric parameters, part 2: feed-horn blockage conditions, *IEEE Antennas and Propagation Magazine*, vol. 45, no. 6 December 2003, pp. 86–89.
51. D. T. Thomas, Design of multiple-edge blinders for large horn reflector antennas, *IEEE Transactions on Antennas and Propagation*, vol. AP-21, no. 2, March 1973, pp. 153–158.
52. S. R. Jones and K. S. Kelleher, A new low noise, high gain antenna, *IEEE International Convention Record*, March 1963, pp. 11–17.
53. C. Dragone, Offset multireflector antennas with perfect pattern symmetry and polarization discrimination, *Bell System Technical Journal*, vol. 57, no. 7, September 1978, pp. 2663–2684.
54. C. Granet, Designing classical dragonian offset dual-reflector antennas from combinations of prescribed geometric parameters, *IEEE Antennas and Propagation Magazine*, vol. 43, no. 6, December 2001, pp. 100–107.
55. T. Li, A study of spherical reflectors as wide-angle scanning antennas, *IEEE Transactions on Antennas and Propagation*, vol. AP-7, no. 4, July 1959, p. 223–226.
56. R. Woo, A multiple-beam spherical reflector antenna, *JPL Quarterly Technical Review*, vol. 1, no. 3, October 1971, pp. 88–96.
57. A. W. Love, Spherical reflecting antennas with corrected line sources, *IEEE Transactions on Antennas and Propagation*, vol. AP-10, no. 5, September 1962, pp. 529–537.
58. F. S. Bolt and E. L. Bouche, A Gregorian corrector for spherical reflectors, *IEEE Transactions on Antennas and Propagation*, vol. AP-12, no. 1, January 1964, pp. 44–47.
59. A. S. Dunbar, Calculation of doubly curved reflectors for shaped beams, *Proceedings of IRE*, vol. 36, no. 10, October 1948, pp. 1289–1296.
60. R. S. Elliott, *Antenna Theory and Design*, Prentice-Hall, Englewood Cliffs, NJ, 1981.
61. T. F. Carberry, Analysis theory for the shaped beam doubly curved reflector antenna, *IEEE Transactions on Antennas and Propagation*, vol. AP-17, no. 2, March 1969, pp. 131–138.
62. V. Galindo, Design of dual reflector antennas with arbitrary phase and amplitude distributions, *IEEE Transactions on Antennas and Propagation*, vol. AP-12, no. 4, July 1964, pp. 403–408.
63. W. F. Williams, High efficiency antenna reflector, *Microwave Journal*, vol. 8, July 1965, pp. 79–82.
64. C. Collins, Shaping of subreflectors in Cassegrainian antennas, *IEEE Transactions on Antennas and Propagation*, vol. AP-21, no. 3, May 1973, pp. 309–313.
65. V. Galindo-Israel and R. Mittra, Synthesis of offset dual shaped subreflector antennas for control of Cassegrain aperture distributions, *IEEE Transactions on Antennas and Propagation*, vol. AP-32, no. 1, January 1984, pp. 86–92.
66. J. J. Lee, L. I. Parad, and R. S. Chu, A shaped offset-fed dual-reflector antenna, *IEEE Transactions on Antennas and Propagation*, vol. AP-27, no. 2, March 1979, pp. 165–171.
67. M. E. Mortenson *Geometric Modeling*, Wiley, New York, 1985.
68. C. C. Han and Y. Hwang, Satellite antennas, Chapter 21 in Y. T. Lo and S. W. Lee, eds., *Antenna Handbook*, Van Nostrand Reinhold, New York, 1993.
69. H.-H. Viskum, S. B. Sørensen, and M. Lumholt, *User's Manual for POS4*, Ticra, Copenhagen, 2003.